IDEALIZED MODELING OF THE ROLE OF STABILITY AND SHEAR ON MESOSCALE GRAVITY WAVE EVOLUTION

BY

MICHELLE M. PITCEL

THESIS

Submitted in partial fulfillment of the requirements
for the degree of Master of Science in Atmospheric Sciences
in the Graduate College of the
University of Illinois at Urbana-Champaign, 2010

Urbana, Illinois

Advisers:

Professor Robert Rauber
Research Scientist Brian Jewett
Professor Greg McFarquhar

Abstract

Mesoscale Gravity Waves (MGWs) are large pressure perturbations that form in the presence of a stable layer at the surface either behind Mesoscale Convective Systems (MCSs) in summer or over warm frontal surfaces behind elevated convection in winter. MGWs are associated with damaging winds, moderate to heavy precipitation, and occasional heat bursts at the surface. The forcing mechanism for MGWs in this study is hypothesized to be evaporative cooling occurring behind a convective line. This evaporatively-cooled air generates a downdraft that then depresses the surface-based stable layer and causes pressure decreases, strong wind speeds and MGW genesis. Using the Weather Research and Forecast Model (WRF) version 3.0, evaporative cooling is simulated using an imposed cold thermal. Sensitivity studies examine the response of MGW structure to different thermal and shear profiles where the strength and depth of the inversion are varied, as well as the amount of wind shear. MGWs are characterized in terms of response variables, such as wind speed perturbations (U′), temperature perturbations (T′), pressure perturbations (P′), potential temperature perturbations (Θ′), and the correlation coefficient (R) between U′ and P′. Regime Diagrams portray the response of MGW to the above variables in order to better understand the formation, causes, and intensity of MGWs. The results of this study indicate that shallow, weak surface layers coupled with deep, neutral layers above favor the formation of waves of elevation. Conversely, deep strong surface layers coupled with deep, neutral layers above favor the formation of waves of depression. This is also the type of atmospheric setup that tends to produce substantial surface heating at the surface.

Za Moju Babu

Acknowledgements

This project would not have been possible without the assistance and support of many people. I am very grateful to my advisors, Brian Jewett, Bob Rauber, and Greg McFarquhar, each of whom helped tediously with revisions and computing issues. A thank you is also due to the people at The National Center for Supercomputing Applications (NCSA) at U of I, especially Albert L. Rossi and Jay Alameda, for their assistance with the Broker system. I also have to give my thanks to the NSF for their funding assistance under NSF Grant ATM-0413824. I also want to thank the entire Department of Atmospheric Sciences at U of I for the opportunity to further my education within the field I love. Last but not least, I would like to thank my family and friends, especially my husband, Cameron, my sister, Sabrina, my Baba, Ane, and my parents, Ronald and Katerina – without your love and support, I would not be where I am today and I am eternally grateful to you.

Table of Contents

Chapter 1: Introduction

The goal of BAMEX, the Bow Echo and Mesoscale Convective Vortex Experiment, was to understand mesoscale processes within Mesoscale Convective Systems (MCSs), and specifically within bow echoes, severe windstorms, mesoscale vortices, and gravity waves. One of the goals of BAMEX was to provide an explanation for the formation of mesoscale gravity waves (MGWs) that occur in the presence of strong straight-line winds beneath the trailing stratiform region of MCSs with a strong stable layer, caused by strong downdrafts generated due to evaporative cooling. It is the objective of this research to quantify the influence that low-level stability, stable inversion layer and forcing layer depth, and wind shear have on the formation, maintenance and amplitude of these types of MGWs.

MGWs are atmospheric waves with wavelengths that range from about 30 to 250 km, periods between 0.5 and 4 hours, and amplitudes that can exceed several millibars (Rauber, et. al. 2001). Pressure perturbations associated with MGWs in the warm season are often associated with the rear portion of mesoscale convective systems (MCSs, e.g. Johnson and Hamilton 1988, Houze et al. 1989), and in the cool season to the rear of elevated convective lines over warm fronts (Browning, et. al. 2000). Severe weather associated with MGWs tends to be somewhat overlooked by the operational community since they trail behind precipitation areas where severe weather is not normally expected to occur (Gaffin 1999). Observations show that MGWs frequently occur in the wake of the precipitation produced in MCSs, and that the waves can cause high wind gusts at the surface. There are many different theories that have been developed to explain the formation of these waves which are outlined in Section 2 of this Thesis. In this thesis, the

hypothesis that MGWs develop as the direct result of evaporative cooling aloft is examined (Lindzen 1974, Raymond 1984, Jewett, et. al. 2003).

The hypothesis that evaporation aloft produces a downdraft that impacts a storm generated cold pool, hereafter generically referred to as the stable layer, in the form of a single pulse of cold air is tested within this thesis. It is hypothesized that such a downdraft would cause a depression in the height of the stable layer, resulting in a drop in the observed surface pressure, which is dynamically similar to that observed in a Wake Low (Johnson and Hamilton 1988, Houze et al. 1989). Highly correlated wind and pressure fields are the primary indicator for the existence of the MGW (Rauber, et. al. 2001, Jewett, et. al. 2003). From the origin of the MGW, secondary waves may radiate outward. This study will focus upon MGWs generated through this process.

The above hypothesis was tested by conducting a modeling study. Simulations were conducted using the Weather Research and Forecast (WRF) model version 3.0 (Skamarock, et. al. 2008). The model was run a total of 1280 times through the use of a batch system, with each model run consisting of a 60 minute simulation. Simulations were implemented by use of UIUC developed software known as the NCSA/LEAD Workflow Broker System (Jewett et al. 2008, Alameda et. al. 2008). The simulations used idealized soundings. For each simulation, the atmospheric lapse rates, wind speeds, and/or layer depth were set at different values. The lapse rates were defined as $\Gamma=\partial\theta/\partial z$. Γ_1 was the surface stable layer with an upper boundary defined as H_1. Γ_2 was the lapse rate above the inversion layer with an upper boundary defined as H_2. Γ_3 was the next lapse rate in elevation with an upper boundary defined as H_3. Γ_4 was the highest specified lapse rate in elevation whose upper boundary was the top of the model domain. Only Γ_1

and Γ_2 were varied in the simulations. Wind shear was varied from the surface up to 700m, and was constant from that height above that level to the top of the model domain. Model generated data fields were saved every minute of model time. Plots of fields such as wind, pressure, potential temperature, and the U′-P′ correlation coefficient gave both a visual representation of the model data and allowed for the creation of what is referred to hereafter as regime diagrams.

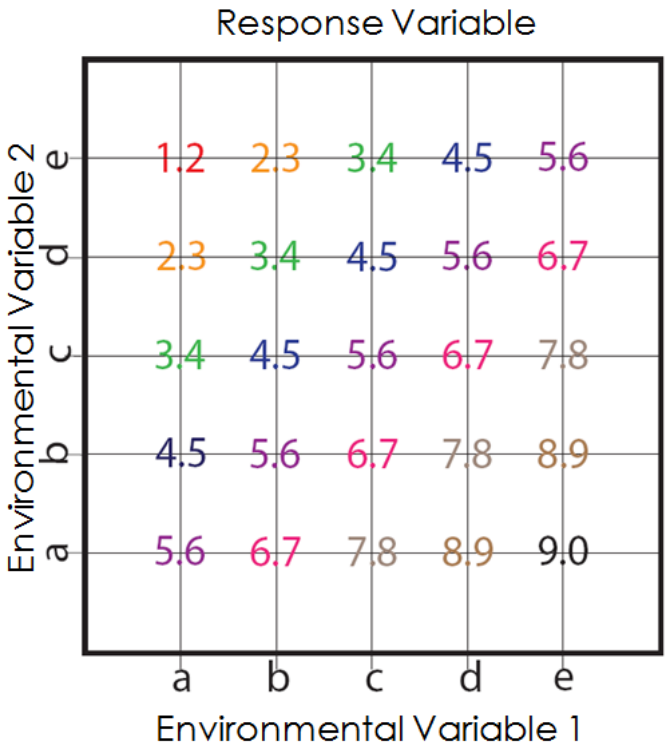

Figure 1. Example of a Regime Diagram. The x-axis is one environmental variable. The y-axis is another environmental variable. The plotted numerical value that occurs as dependent upon both variables is the response variable.

Regime diagrams plot the value of the response variable as a function of two environmental variables (Figure 1). Environmental variables consist of the first two lapse rates and their associated depths. These diagrams will be used to assist in determining the wave response to physical forcing and environmental conditions.

The remainder of the thesis is organized as follows. Chapter 2 contains a literature review of the prominent theories surrounding MGW formation and evolution. Chapter 3 describes the model simulations and the methodology through which the outputs are analyzed. In Chapter 4, the model results are presented and discussed. This is followed by the conclusions in Chapter 5.

Chapter 2: Literature Review

Sharp surface pressure perturbations frequently occur within mesoscale weather systems. Perturbations as large as 10mb can occur within several minutes, and are accompanied by rapid fluctuations in surface winds (Rauber, et. al. 2001). Pressure perturbations in the warm season are often associated with mesoscale convective systems (MCSs, e.g. Johnson and Hamilton 1988, Houze et al. 1989), and in the cool season with elevated convection moving over warm fronts (Browning, et. al. 2000). MGWs have been observed to occur with a surface-based stable layer present, one example of which is lower-level tropospheric inversions found north of a warm front (Uccellini and Koch 1987). Figure 2 depicts an example of these pressure perturbations common in both.

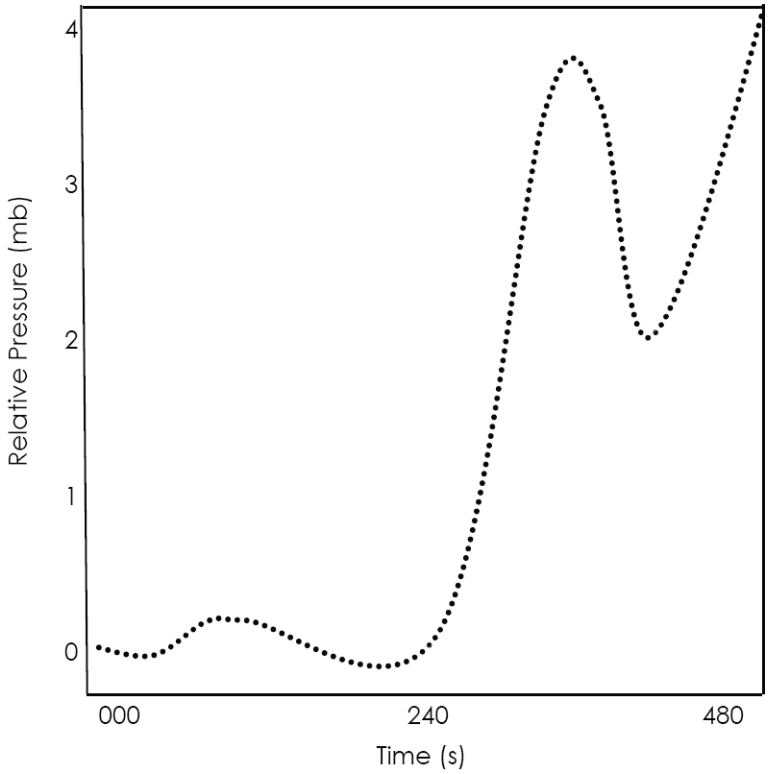

Figure 2. Example of sharp pressure perturbations over a warm front as would appear on a barograph, based upon Rauber, et. al. (2001).

Pressure perturbations within MCSs can be associated with wake lows beneath the trailing stratiform regions (e.g. Johnson and Hamilton 1988, Houze et al. 1989). The wake low, as illustrated in Figure 3, forms as downdrafts in evaporatively-cooled air beneath the MCS anvil descend, warm dry adiabatically, and depress the upper surface of the storm-generated cold pool. Storm relative surface winds are divergent ahead of the low, convergent behind the low, and maximum at the position of the low (Johnson and Hamilton 1988).

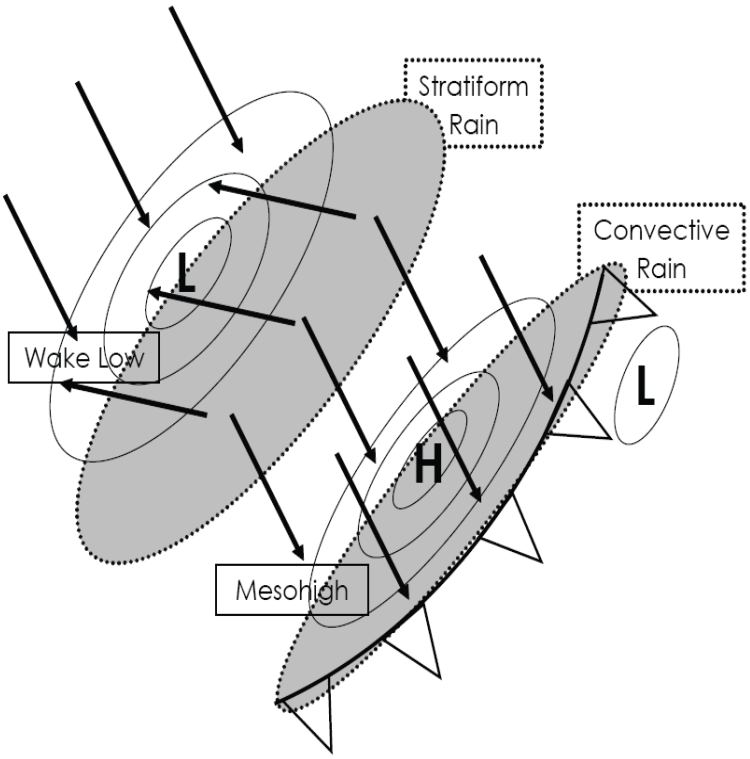

Figure 3. Mesohigh-Wake Low Couplet. Black arrows denote wind direction. Grey shaded areas denote areas of precipitation.

The pressure perturbations within MGWs have wavelengths that can range from 30 to 250 km, have periods between 0.5 and 4 h, and amplitudes that can exceed several millibars in surface pressure (Rauber, et. al. 2001). The amplitude and period of MGWs coincide well with those of high-frequency surface pressure perturbations that are

associated with MCSs (Browning, et. al. 2000). In the area near to the surface, MGWs associated with MCSs and elevated convection over stable layers have been identified from time series observations of surface pressure (p) and wind. MGWs also can be the driving force for strong and highly localized precipitation bands, and can be the trigger for damaging surface winds (Eom 1975; Bosart and Sanders 1986; Rauber, et. al. 2001). The hypothesized structure of MGWs associated with elevated convection over a cold pool or frontal stable layer that is the basis for this thesis is illustrated within Figure 4.

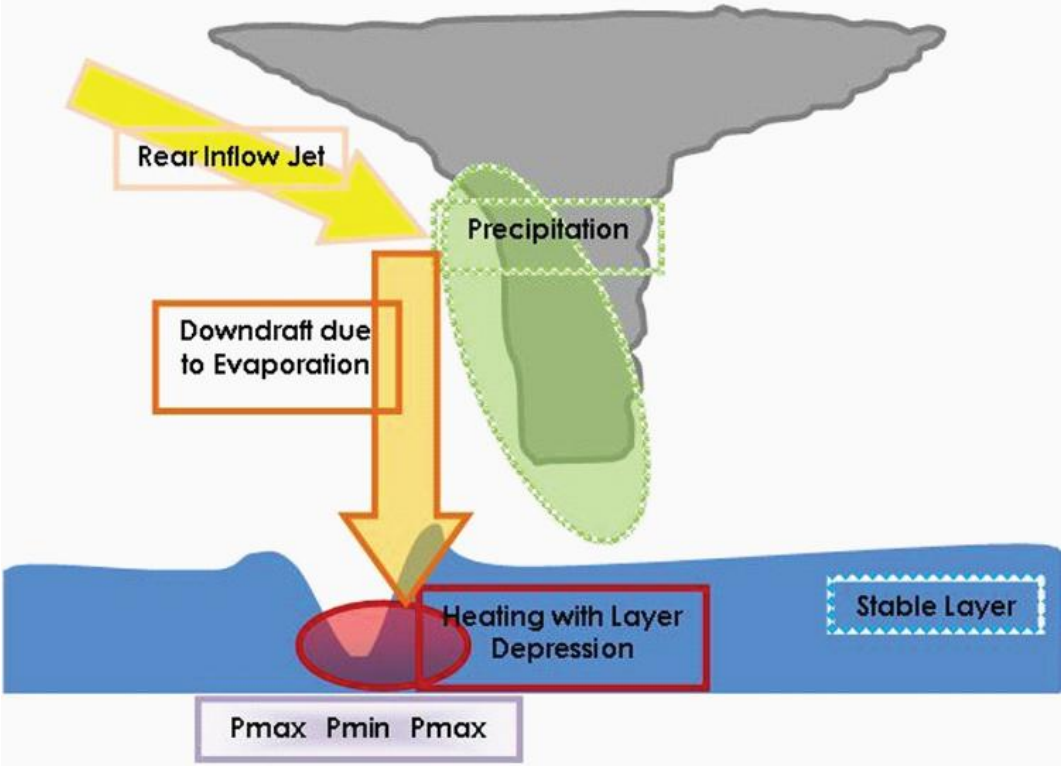

Figure 4. Hypothesized MGW environment with elevated convection over a stable layer.

MGW wave activity can occur in wave packets or as singular waves that are associated with frontal zones, precipitation bands, squall lines, hailstorms, and heavy snowstorms (Uccellini and Koch 1987). MGWs have been observed with lifetimes

several hours long as well as lengths of travel over 100km (Ferguson 1967; Bosart and Cussen 1973; Lin and Goff 1988; Rauber, et. al. 2001).

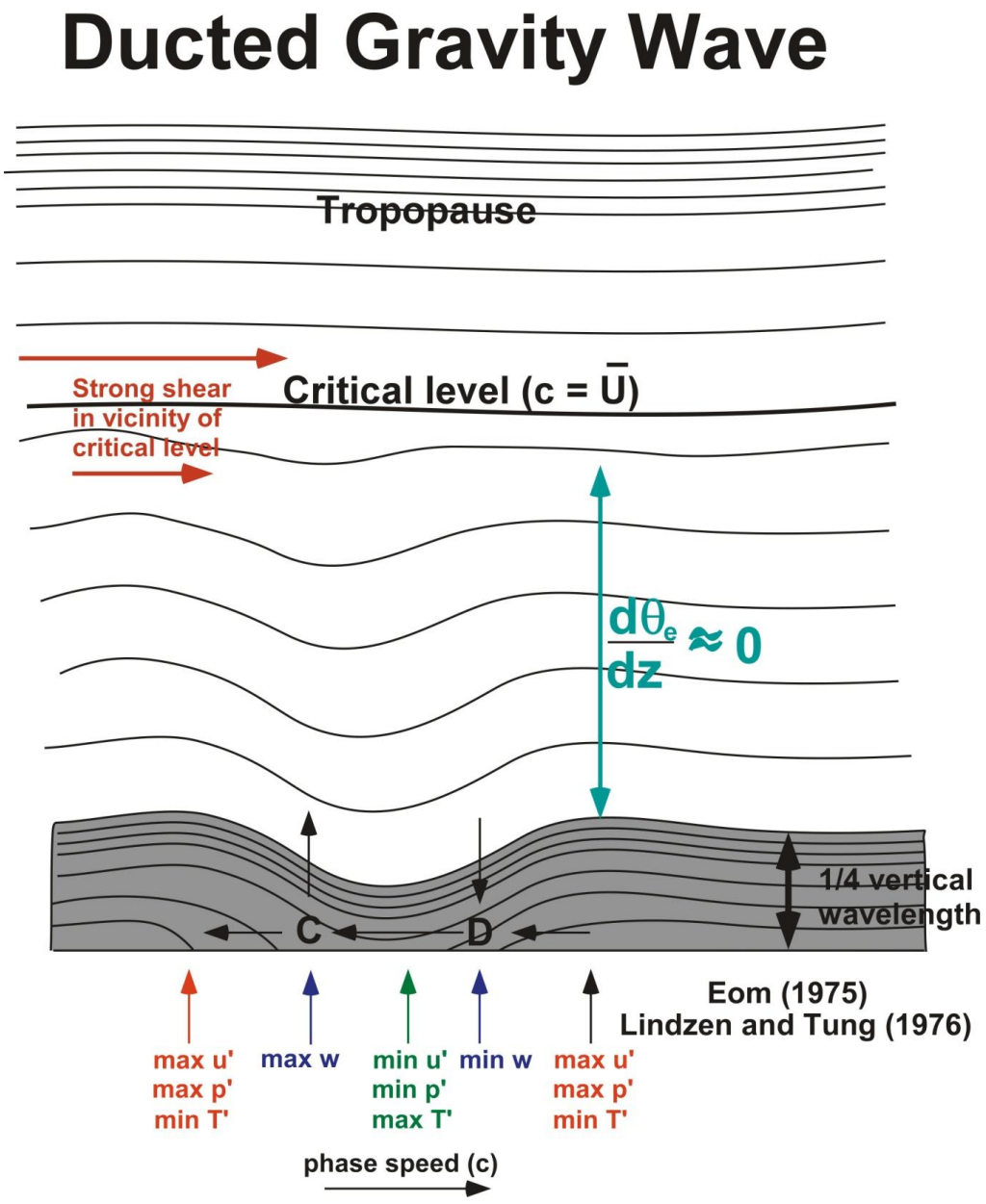

Figure 5. Ducting as a mechanism for lengthening the lifetime of MGWs. The surface stable layer is shaded in grey. The layer above the stable layer is neutral.

Ducts may prolong the life of MGWs (Lindzen and Tung 1976; Browning et. al. 2000). However, without a duct through which they can travel or some form of continuous forcing, this life-time would be considerably shortened as the wave moves away from its genesis region. An atmospheric duct acts as a channel, through which the MGW can propagate away from its source region with minimal loss of energy (Uccellini and Koch 1987; Browning et. al. 2000). Ducting is portrayed in Figure 5. A duct requires a low-level inversion with a critical layer, a level of low Richardson number less than 0.25 near the critical level, and a neutral layer immediately above the inversion (Lindzen and Tung 1976). The critical layer is a level in which the wave speed matches the background environmental flow. This critical layer, which is generally above the surface inversion, should have a depth of one half the vertical wavelength of the MGW. The critical level is the topmost boundary of the critical layer. The stable layer should also have a depth greater than or equal to one quarter of the vertical wavelength of the wave (Lindzen and Tung 1976).

MGWs can be caused by a number of mechanisms. One mechanism for MGW formation involves vertical shearing instability. This vertical shear environment may be the result of a jet streak occurring in congruence with an associated critical level and a region of low Richardson number less than 0.25 (Booker and Bretherton 1967; Gossard and Hooke 1975). This critical level would allow for the passage of potential energy to occur between the mean flow and the MGWs (Rosenthal and Lindzen 1983a, b; Stobie et al. 1983; Ramamurthy et. al. 1993). Pecnick and Young (1984) found that the conversion of energy and motion from the mean flow to the wave is much larger near the critical level, where large shear and smaller static stability represent an area of minimum

Richardson number. This enhances the prospect that this is an area of MGW genesis. After formation, some waves would propagate away from the region of genesis, while others may remain connected to their forcing mechanism.

Another mechanism involves a preferred synoptic setting. This preferred synoptic setting for MGW formation has been identified from past observational and modeling studies. The pattern, as described by Uccellini and Koch (1987), consists of a surface cyclone with a warm front and a surface level inversion, coupled with a negatively-tilted 300mb trough and jet streak, with or without precipitation. A negatively tilted trough occurs with mature low pressure systems with strong vertical wind shear concurrent with an area of strong differential advection. The system is bounded on the east by a ridge axis and on the west by an inflection point between the upper-level ridge and trough (Van Tuyl and Young 1982). A similar configuration is seen at 500mb as well (Schaub 2005, Uccellini and Koch 1987).

As a jet streak approaches the upper-level ridge, an unbalanced situation is hypothesized to develop which results in a significant increase in the upper-level wind divergence (Uccellini, et. al. 1987). Highly diffluent flow at 300mb occurs due to the geostrophic adjustment process that forms in response to the unbalanced flow. Geostrophic adjustment is a process which involves a redistribution of momentum and mass through gravity-inertia waves (Ramamurthy et. al. 1993). As geostrophic adjustment is occurring, the area to the north of the warm front is the areas that favors MGW genesis, as was discussed in the data from STORM-FEST (Jewett, et. al. 2003; Schaub 2005). Figure 6 depicts the unbalanced flow that occurs in the vicinity of the jet streak during the geostrophic adjustment period.

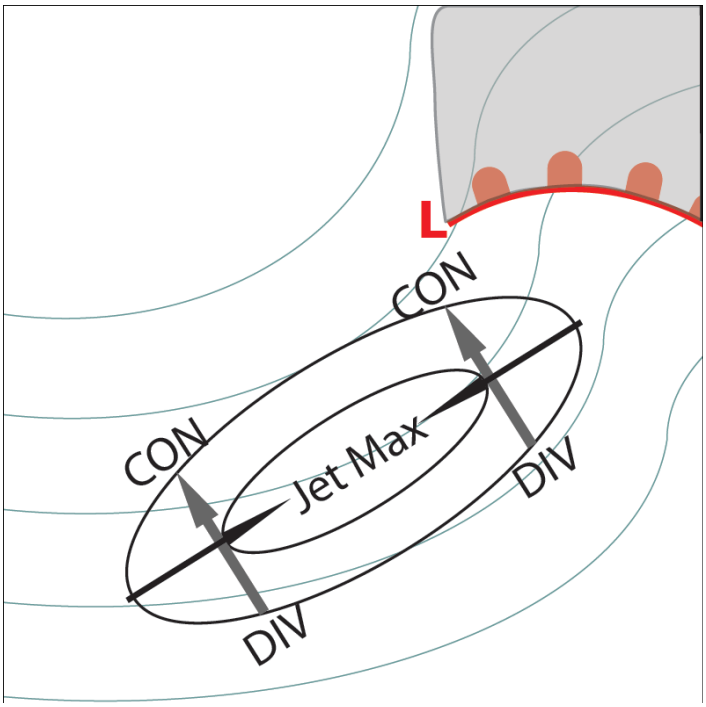

Figure 6. Ageostrophic flows hypothesized to occur near to a jet streak when the flow is significantly imbalanced. Grey arrows denote the ageostrophic flow. Unbalanced flow exists in the exit region of the jet. Black arrows denote the acceleration vectors, pointing towards the jet maximum. The Low pressure system coincides with the right exit region of the jet.

When large Rossby numbers are observed with prominent jet streaks, the quasi-geostrophic and balance theories dictate that the secondary circulations created would destroy the prior balanced condition (Van Tuyl and Young 1982). An increase in the upper-level wind divergence is hypothesized to occur as the jet streak moves near to the upper-level ridge, causing an unbalanced flow to form that would trigger the geostrophic adjustment process that forms the MGWs (Uccellini et al. 1984; Ramamurthy et. al. 1993; Van Tuyl and Young 1982). Unbalanced flow is indicated by, but not limited to opposite-normal ageostrophic winds that exist in the exit region of a geostrophic wind maximum and the values for the Lagrangian Rossby number exceeding 0.5 in a region where the winds in the jet maximum are greater than $1ms^{-1}$ (Koch and Dorian 1988).

Another possibility for MGW formation is frontal collapse. This mechanism is most likely an attempt by the atmosphere to return to geostrophic balance. After semi-geostrophic frontal collapse, gravity waves form (Snyder et. al. 1993).

With frontogenesis, a sequence of gravity waves may form directly above the frontal surface and move with the front, keeping the waves stationary relative to the frontal system. MGW formation is hypothesized to result when the frontogenetical forcing is strong and induces rapid changes to the thermal wind balance. Additionally, in the cross-frontal circulation, the largest deviations from semi-geostrophic balance are hypothesized to produce gravity waves (Snyder et. al. 1993). The formation of smaller wavelength MGWs on the order of 30 km have been initiated by areas of vertical shear within cold frontal zones (Testud et al. 1980; Parsons and Hobbs 1983) and already existing thunderstorms and their associated stratiform precipitation areas (Ley and Peltier 1981).

It has been suggested that MGWs cause convection (Uccellini 1975; Stobie et al. 1983). Eom (1975) proposed a linear model of gravity waves that Uccellini (1975) applied in a case study to atmospheric soundings, whose results showed that the waves were capable of generating convection since the waves had the ability to lift parcels to their level of free convection (Schmidt and Cotton 1990, Ramamurthy et al. 1993). Bosart and Sanders (1986) showed that the leading intrusion associated with the moderately high convective tops existed near a propagating surface wind shift associated with a MGW. A striking effect that was observed was the lightning activity that occurred in correlation with the MGW as it traversed along its path, despite the minimal instability for upright

convection was observed. This lends more evidence hereto that the convection was instigated by MGW activity (Bosart and Sanders 1986).

Wave Conditional Instability of the Second Kind, hereafter referred to as wave-CISK, has also been attributed to MGW formation. The wave-CISK hypothesis implies that convection will only impact and manipulate the motion and activity of those parcels of air that are lifted to the level of free convection by boundary layer motions (Raymond 1976). MGWs are able to produce low-level convergence and can respond to the flux of latent heat that is associated with the resulting convection (Lindzen 1974, Raymond 1984). Convection enhances the wave trough by forming waves to balance the sinking of air due to subsidence, and enhancing the wave ridge through the process of evaporative cooling of precipitation.

Additionally, the wave-CISK theory shows that the strongest convective updrafts occur at the wave critical level, which implies that the MGW and the convection will move together through the atmosphere as they are inherently connected and dependent on each other (Koch and Golus 1988, Cram 1992). Koch and Handley (1997) showed this dual movement through the examination of isentropic cross sections aligned normal to the MGW. Although MGWs and wave-CISK theory can display somewhat different profiles of vertical motion through isentropic analysis, it can be assumed that the convection that develops would not change the phase relationships between the temperature, pressure, and wind perturbations that are observed with MGWs (Koch et al. 1988, Powers and Reed 1993, Koch and Handley 1997).

MGW formation may also be caused by convection. From manual analysis of 1038 large pressure perturbations in the contiguous United States, Koppel et al. (2000) showed that MGWs in the stratiform region may form as a result of convective activity in the atmosphere. This mechanism acts similarly to the way in which MGWs form in the wake low in MCSs. Atmospheric motions, such as convection, may also enhance existing MGWs (Ferguson 1967; Bosart and Cussen 1973; Lin and Goff 1988; Rauber, et. al. 2001).

In a modeling study, Powers and Reed (1993) further showed the correlation between convection and MGW genesis. When latent heating was included within their model simulations, MGWs formed. However, when the effects of latent heating were removed, the MGWs were not generated. A similar effect was observed in the modeling study by Jewett et al (2003). With the effects when latent cooling omitted, the MGW activity failed to present itself, despite MGW formation being previously observed when latent heating was included.

Powers (1997) demonstrated in their modeling study that elevated convection moving concurrent with MGWs can represent a continuous forcing mechanism, suggesting convection can maintain some MGWs. By strengthening the wave, which may in turn strengthen the convection, waves are created in response to the localized ascent of updrafts or forcing by downdrafts. At the highest point of the stable layer, the MGW structure is similar to those of trapped waves at low levels associated with elevated convective cells.

There is a striking similarity between the behavior of mesohigh-wake low couplets in MCSs and the area ahead of warm fronts and the behavior that is observed with MGWs. The forcing in these phenomena appears to be the evaporative cooling that occurs to the rear of the convective line in the stratiform region of the MCS, providing the means for MGW and the associated mesohigh-wake low couplets to form. Additionally, since the surface perturbation and wind fields accompanying the mature gravity wave in the model strongly resemble the mesohigh and wake low accompanying an MCS (Jewett, et. al. 2003), an easy way to envision the pattern of pressure perturbations associated with MGWs is the mesohigh-wake low signature. This couplet is a quasi-steady-state linear response to low-level cooling that is associated with an area of stratiform precipitation (Haertel, et. al. 2000).

The proposed hypothesis that evaporation aloft produces a downdraft that impacts a stable layer, thereby leading to the formation of an MGW, is the subject of this thesis. In nature, the forcing is continuous as cold air descends beneath the evaporation region of the trailing stratiform cloud and impacts the inversion. In this thesis, a simplification of this process is tested. A single pulse of cold air was produced in the model, dropped on the inversion, and subsequently produced MGW activity.

The end goal of this study is to understand the relationship between MGW evolution and certain environmental variables. These variables include the lapse rate within and above the stable layer, the depth of the surface stable layer, the depth of the layer in which evaporation occurs, the variance of wind shear in the model domain, and the magnitude of the evaporative cooling aloft. As these variables change between the different simulations, certain key response variables should appear. A correlation

between U′ and P′ is one of these that will be calculated. If MGW activity is truly occurring within the model, then a positive correlation between u’ and p’ is expected. Additionally, changes in the overall surface winds and the measured temperature in the vicinity of large pressure changes should occur as a result of MGW activity.

Chapter 3: Methodology

The conditions under which MGWs form and evolve were assessed through a series of idealized numerical simulations. Changes to the depth and strength of the stable layer at the surface, and the stability and depth of the air above the surface stable layer, were made to determine environments that are most prone to MGW formation. As the model is dry, an imposed cold source aloft simulates the evaporational cooling that would normally occur in nature and allow for the wave development. Additionally, each simulation has some amount of shear, which displaces this imposed cold source toward the east, which allows the inversion to recover from the impact depression of the stable layer produced by the downdraft. By allowing for shear to somewhat displace the cold source and the resultant waves, the waves generated in the model were able to travel some distance. Generally, a depression of the inversion immediately followed behind the cold source, which is equivalent to what occurs in a storm with an evaporatively-driven downdraft above a stable layer.

Simulations were conducted using the Weather Research and Forecast (WRF) model version 3.0 (Skamarock, et. al. 2008). The model is nonhydrostatic. The model dynamics make use of 3rd order Runge-Kutta operations. The dynamics parameterization that was used for this study is Eddy Coefficient Option 2, which employs the use of turbulent kinetic energy. The sensitivity tests were carried out using a single grid with 1 km by 1 km horizontal resolution with 41 evenly spaced vertical levels, with periodic boundaries to help reduce spurious waves in the model domain. The x-domain was 250 km, the y-domain was 100 km, and the z-domain was 20 km. Upper level Rayleigh

damping is used with the damping depth set to 5 km. An example image portraying the x-y coordinates is shown in Figure 7.

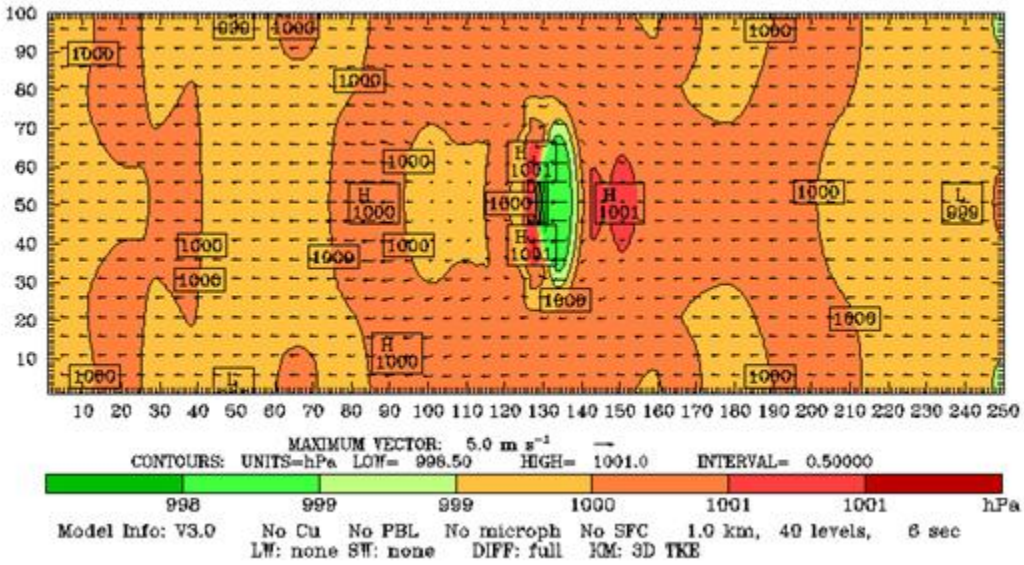

Figure 7. Image of surface pressure depicting the horizontal coordinates of the model domain.

There is always the danger that spurious waves might occur within modeling simulations. According to Lindzen and Fox-Rabinovitz (1989), there are several issues that must be addressed to reduce problems associated with spurious waves. Most models suffer from some noise that originates from unsmoothed, damped model output data, whether it is real or generated. The use of smoothing and damping can decrease the horizontal and vertical resolutions (Lindzen and Fox-Rabinovitz 1989) by smoothing away finer scale features that appear in the model data. The author is aware of all these issues and has taken steps to help try to ensure that they are not directly an issue in this study, by means of choosing an appropriate damping setting within the model.

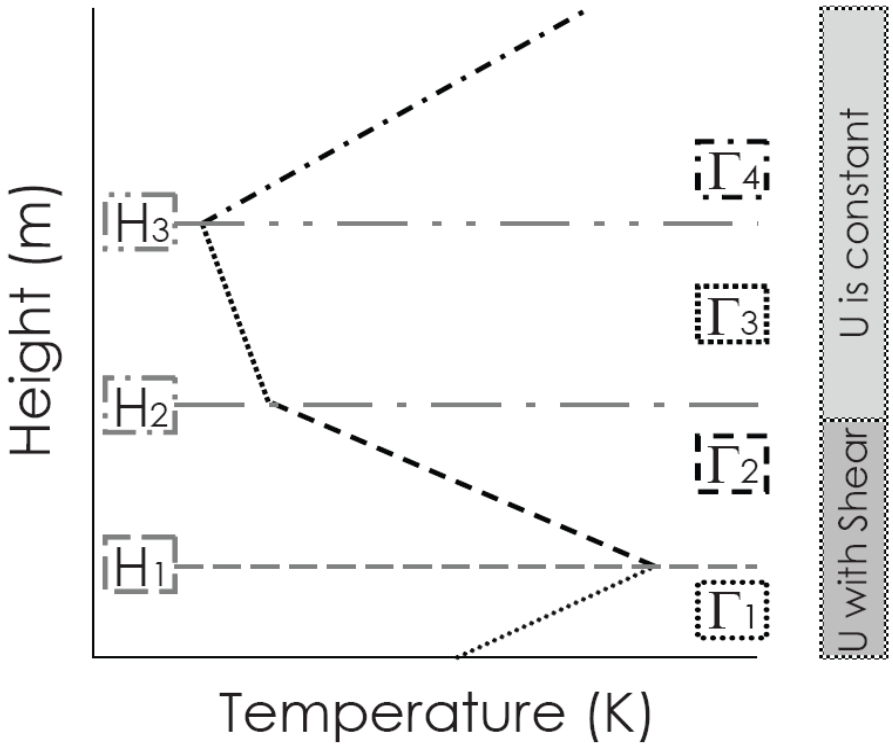

Figure 8. Generic sounding setup for all simulations.

The model was initialized using idealized soundings with varying stability near the surface in environments that are initially horizontally uniform in terms of temperature, wind speed, and pressure. The use of idealized soundings is useful to determine which environments prove more conducive to MGW formation. The idealized soundings had a surface based inversion, above which a less stable layer existed. This is depicted in Figure 8. The east-west (or "x-direction") background wind speed "U" was varied. The control model runs had initial wind speeds set at 0 m/s so that the only winds generated in the model were by the action of the descending cold pulse. For the other three sets of model runs, the U-wind began at -5m/s at the surface and, depending upon the amount of shear, increased to 10m/s, 20m/s, or 30m/s at 700.0 m. The background U was set as constant from 700m to the top of the model. These values were chosen to allow for a variety of wind shear environments within the model and were based on

several real-world soundings. The north-south (or "y-direction") wind speed "V" was initially zero and only varied as a direct response of the action of the descending cold pulse. The mixing ratio was 0 kg/kg. The surface temperature was initially a constant 283.15 K. The atmosphere was divided into four layers so that the depth and lapse rate within different atmospheric layers could be varied independently. The height of the Tropopause was set to H_3.

The lapse rates were defined as $\Gamma=\partial\theta/\partial z$, as Figure 8 portrays. The values were determined by examination of real world and simulated soundings to find a valid range upon which to vary the lapse rates. The lapse rate in the inversion layer, Γ_1, ranged from 8-14.0K/km. The top of Γ_1 was defined as H_1, and ranged from 300-1800m. Γ_2 was the lapse rate above the inversion layer, and ranged from 0-6.0 K/km. The top of the layer with this lapse rate, H_2, was defined as H_1+1000.0m - H_1+3000.0m. Γ_3 was the lapse rate of the next layer aloft, and had a constant value of 3K/km for all simulations. The top of the layer with this lapse rate, H_3, was defined as 10000m. Γ_4 was the lapse rate of the highest layer in elevation and had a constant value of 17K/km for all simulations to mimic lapse rates within the stratosphere.

A cold source was placed above the second layer. This imposition of a cold bubble is used as the catalyst to start the MGW activity since the model uses dry physics with no boundary layer. This cold source had a perturbation value of -10 K to the environment. The strength of the downdraft, which is caused by the colder air above H_2, is of great interest as it serves as the trigger mechanism for MGW formation on the stable layer.

The model was run 1280 times, with each model run 60 minutes long. Simulations were implemented by use of UIUC developed software known as the NCSA/LEAD workflow broker system (Jewett et al. 2008, Alameda et. al. 2008). The broker system is useful in the development of batch jobs, monitoring the status of the individual jobs, and the creation of images and output from the model results. The use of the broker allowed hundreds of simulations to be completed for a wide range of low-level stability and imposed cooling aloft. This batch system systematically changed the values of the different variables that are used to create the idealized sounding, as well as the value of the elevated cold source. These variations provided many different scenarios for MGWs to form. The variables are summarized in Table 1 below.

Environmental Variables	**Range**	**Increment**	**Multiplier**
Γ_1	8 – 14K/km	by 2	4
H_1	300 – 1800m	by 500	4
Γ_2	0 – 6K/km	by 2	4
H_2	1000 – 3000m	by 500	5
Γ_3	3K/km	n/a	1
H_3	10000m	n/a	1
Γ_4	17K/km	n/a	1
Shear	0 – 30 m/s	by 10	4
		TOTAL	**1280**

Table 1. Summary of variables manipulated in the model by the Broker system. The column titled "Multiplier" refers to the number of values that occur for each Environmental Variable due to the number of incriminations that they undergo.

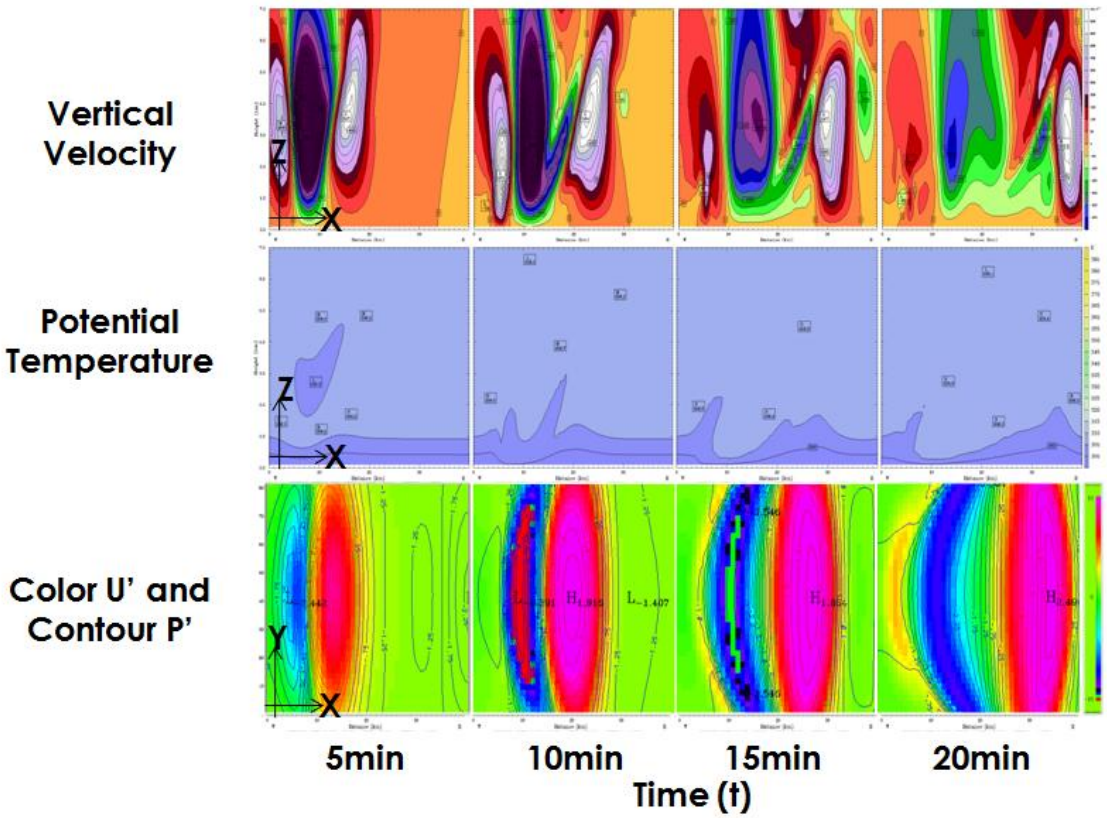

Figure 9. The generic lifecycle of an MGW. A cross-section of vertical velocity is depicted in the top row, with cooler colors signaling downward movement and warmer colors signaling upward movement. A cross-section of potential temperature is depicted in the second row, which symbolizes the stable layer and the falling thermal. The bottom row depicts a plan-view of color-filled U′ and contoured P′. Tim is as indicated along the bottom of the image.

The lifecycle of a MGW should yield a set of expected results based upon the response variables. A general idea of this lifecycle is presented in Figure 9. If a MGW forms, the following should be visible in the model data. With vertical velocity, there should be an initial downdraft with associated updrafts on either side. This should coincide with an area of lowered pressure with heightened pressure on either side. Additionally, the lowering of pressure should have associated areas of heightened pressure on the leading side if shear is introduced into the model. Wind should be correlated with the changes in pressure.

Response variables were calculated for each simulation and the correlation coefficient between surface pressure and surface wind perturbations, or changes, was calculated. For the MGWs it was expected that the pressure and wind be positively correlated. Correlation coefficients can vary from -1 to +1, with -1 being a perfect negative correlation and +1 being a perfect positive correlation. The correlation 'r' was calculated using the following set of equations

$$r = \frac{\sigma up}{\sigma u \sigma p} \tag{1}$$

where

$$\sigma u = \sqrt{\frac{(u_n - u_{avg})^2}{n}}\ , \tag{2}$$

$$\sigma p = \sqrt{\frac{(p_n - p_{avg})^2}{n}}\ , \tag{3}$$

and

$$\sigma up = \sqrt{\frac{(u_n - u_{avg})^2 (p_n - p_{avg})^2}{n}} \tag{4}$$

However, it is important to note that the best correlation does not always produce the largest increase in wind or pressure. Due to the mathematical manner in which correlation is calculated, it is possible to produce near-perfect correlation in a simulation where the U′ and P′ are both smaller than one m/s or mb respectfully, or even equal to zero, if the area is unaffected by wave activity. While correlation can be used as a tool to initially detect MGW activity since a wave should have well correlated U′ and P′, it is important to not just assume that good correlation is always indicative of MGW activity, but an indicator that MGW activity may be occurring.

Finally, regime diagrams were created to show how response variables varied as a function of environmental variables. Regime diagrams display the change in one variable as the result of changing inputs to the idealized simulations, and hence help explain conditions conducive to MGW formation. Regime diagrams in this study depend upon the depth and strength of Γ_1, Γ_2, as well as the amount of vertical shear. By developing these diagrams, they may help to serve as a tool to assist in the future research and prediction of when MGW activity associated with convective storms is likely to form, the amplitude of the waves, and the possible resultant severe straight-line winds at the surface.

Chapter 4: Results and Discussion

In this section, results from the idealized sensitivity tests concerning the structure and amplitude of MGWs forming under different environmental conditions are discussed, beginning with the types of behavior that occur at the surface in the wake of a descending cold thermal. Next, MGW behavior, based on one simulation, is presented using visualization of the model results. Regime diagrams are then presented, focusing upon relationships between MGW evolution and surface layer height and stability changes, secondary level height and stability changes, and variance of vertical wind shear. Following this is a discussion of heat burst formation in the model. Finally, an overarching discussion of the findings concerning MGW development is presented.

4.1 Types of Cold Thermal Responses at the Surface

There are four atmospheric responses that are expected as a result of a falling thermal in the modeled atmosphere. The first is a microburst. This type of response is favored when either a neutral or near neutral layer from the surface continues higher up into the atmosphere, as is displayed in Figure 10. This is further enhanced by the existence of minimal to no vertical wind shear (ΔU). In this situation, a cold thermal perturbation descends from aloft and increases its momentum as the neutral layer leads to an acceleration of the downward motion of the thermal. As such, it will increase in speed, eventually impacting the surface where it will spill outward, with a poorly correlated increase in U' and P' and a decrease in T' at the surface. The cold thermal will spread outward at the surface and displace the warmer surface air since the thermal stays colder

than its surroundings. This is contrary to the expected MGW atmosphere in which a stronger, stable layer would be present at the surface.

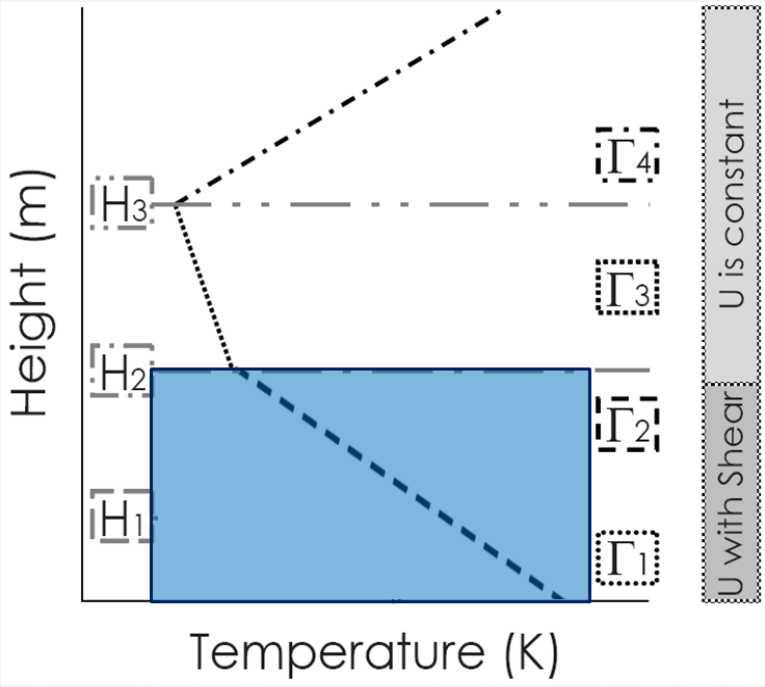

Figure 10. A microburst atmosphere. Layers 1 and 2 are shaded in blue and are assumed to be neutral (Γ=0 K/km). In this situation, if the thermal were released, it would fall uninhibited until it reached the surface where it would cause a microburst.

The second response that may occur is a heat burst. As in the microburst environment, as the cold perturbation descends through the upper neutral layer with minimal shear, it gains momentum. When the cold perturbation reaches the stable layer (layer 1), the thermal will lose negative buoyancy and may become positively buoyant if it passes the level of neutral buoyancy. This resistance can be larger if the stable layer is stronger. This configuration of a stable layer at the surface with a neutral layer above is portrayed in Figure 11. The inversion will bend to the force of the cold thermal. As the thermal falls, it will depress the inversion depth and thus the integrated mass above the surface, causing a hydrostatic pressure fall. As the perturbation sinks into the stable layer,

it heats due to subsidence and compressional warming. If the momentum is strong enough for the cold thermal to evacuate the inversion layer and impact the surface despite having acquired positive buoyancy, a surface heat burst results, manifested as an increase in T′ at the surface.

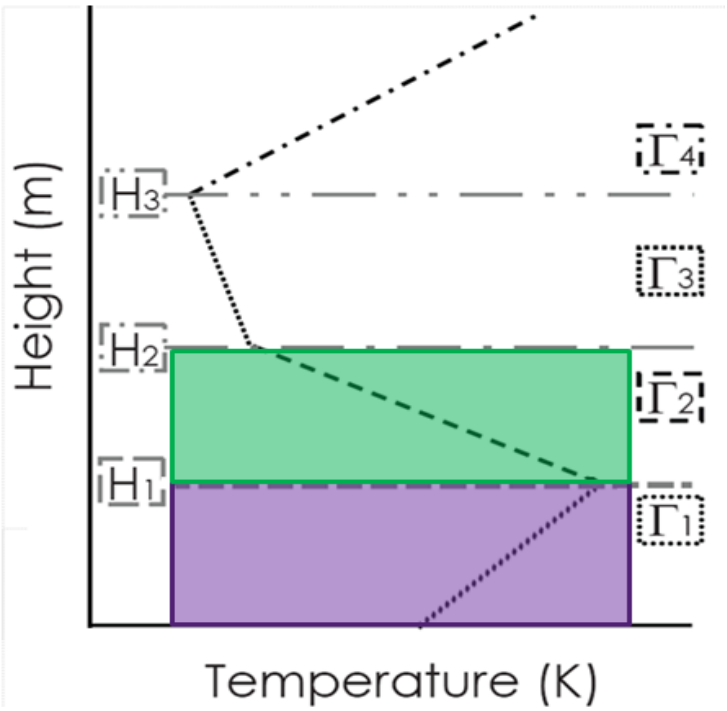

Figure 11. A heat burst atmosphere. Layers 1 and 2 are shaded in purple and green respectfully. Layer 2 is assumed to be neutral (Γ=0K/km), while layer 1 is assumed to be stable.

The third type of response is a stationary wave disturbance with secondary waves radiating from the core. In an atmosphere with no shear under which conditions are best suited for this type of response, the environment for this type of response is found to be similar to that for a heat burst, however layer 1 is more stable and deeper and layer 2 is neutral (Γ_2~0 K/km) or slightly stable. In this situation, if the thermal were released it would fall until it reached Layer 1, where it would begin to decelerate due to resistance by the stable layer. In this wave scenario, the descending thermal would not reach the

surface. The negative buoyancy of the thermal would diminish and the impact would cause a wave depression as indicated by a positively correlated increase in surface U′ and P′ with a possible increase in T′ at the surface. The wave would appear as a continuing pulsation of U′ and P′ at the surface, similar to the way a calm pond looks if a rock is dropped from above, with ripples of waves radiating outward from the point of impact.

The fourth type of response is a MGW that forms in an environment that includes shear. As in scenario three, layer 1 is stable (Γ_1>0K/km) and layer 2 is neutral (Γ_2=0K/km). In this situation, if the thermal were released it would fall uninhibited until it reached Layer 1, where it would begin to decelerate. As this occurs, the negative buoyancy of the thermal would diminish due to the impact with layer 1, but would transport higher horizontal momentum air downward, depositing it in the stable layer. With shear present to organize the wave energy, the MGW would appear as a more solitary wave, propagating in the direction of the shear, with a correlated change of U′ and P′ at the surface. In this situation, the wave would resemble a solitary ocean wave rather than the ripples in a pond.

4.2 Visualization of a MGW

A single simulation that exemplifies the behavior of a MGW in the model is presented in this section. The variables describing this simulation are shear of ΔU = 20 m/s, Γ_1 =14 K/km, H_1 = 1300 m, Γ_2 = 0 K/km, and H_2 = 3000 m.

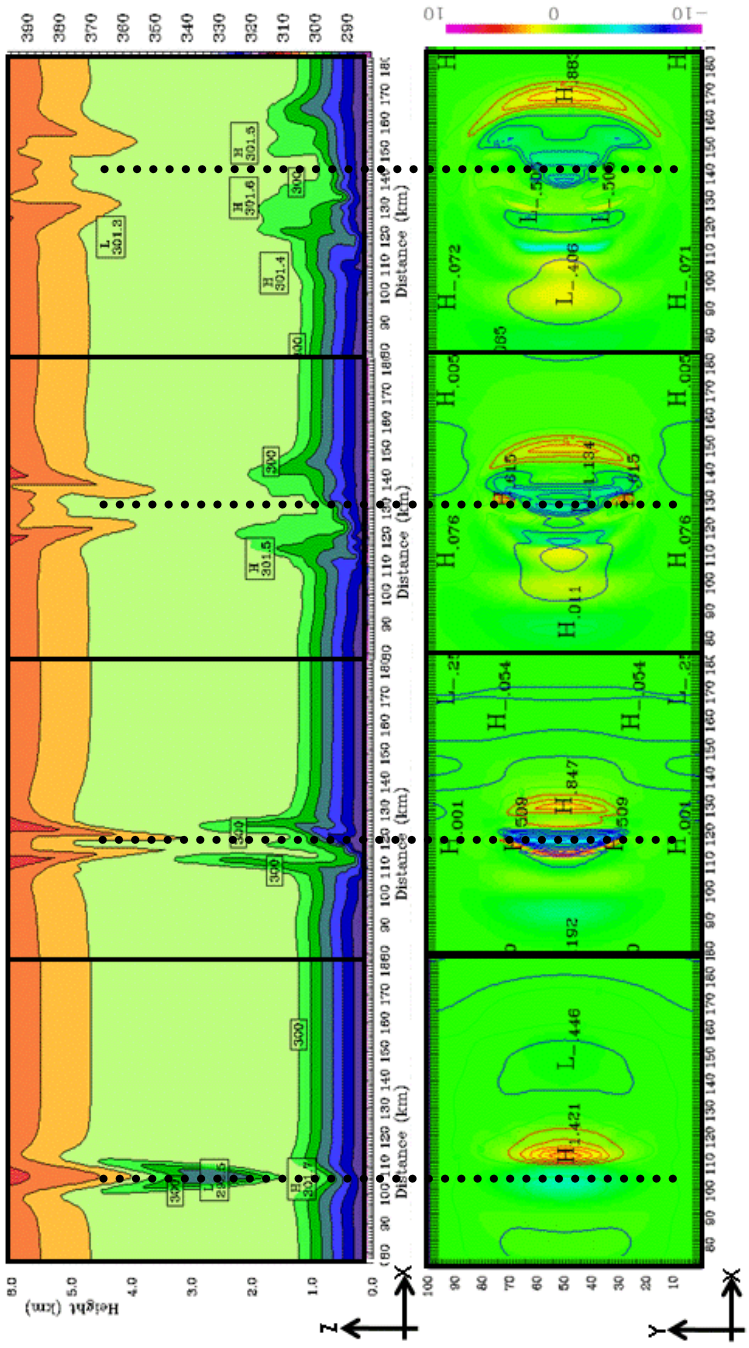

Figure 12. Potential temperature cross-section along the Y center of the domain is presented in the first row. A plan view of surface U′ shaded with P′ contours overlaid are presented in the second row. Images are for 5min, 15min, 25min, and 35min into the simulation. The dotted line at each timeframe indicates the depression of the stable layer and the corresponding decrease in U′ and P′.

Figure 12 details the θ distribution along the Y-center of the domain for 5-35 min at 10 min intervals. The figure shows the cold thermal descending and beginning to impact the stable layer near the surface at 5 min into the simulation. At 15 min, the cold thermal has fully impacted the stable layer and a wave is beginning to move eastward due to the influence of shear. At 25 min the mature wave is progressing away from the point

of impact with a second crest following the first. At 35 min, the wave continues propagating eastward where it continues with much the same profile until the simulation reaches its end at 60 min. For reference, the evolution of the θ field in this figure is similar to the theoretical behavior depicted in Figure 4.

The second row of Figure 12 depicts a plan view of the evolution of surface U′ and P′ for the same times as the first row. The MGW moves 100 km during the wave lifetime. Beginning at 5 min, perturbation wind and pressure fields are forming in response to the forcing instigated by the falling cold thermal impacting upon the surface stable layer. The perturbation is still present at 15 min after the thermal has fully impacted the stable layer. This is evidenced by the lowering of pressure under the impact zone with a correlated decrease in wind speed. Conversely, ahead of the impact zone is a correlated increase in wind speed with an increase in pressure. At 25 min, the perturbation continues to move eastward away from the point of impact while a secondary wave traverses closely behind. The wave continues moving toward the east at 35 min and does so until the simulation completes at 60 min. Point time series reveal correlations throughout the MGW lifetime were about 0.9. For reference, the evolution of U′ and P′ in this figure is similar to the behavior depicted in Figure 13.

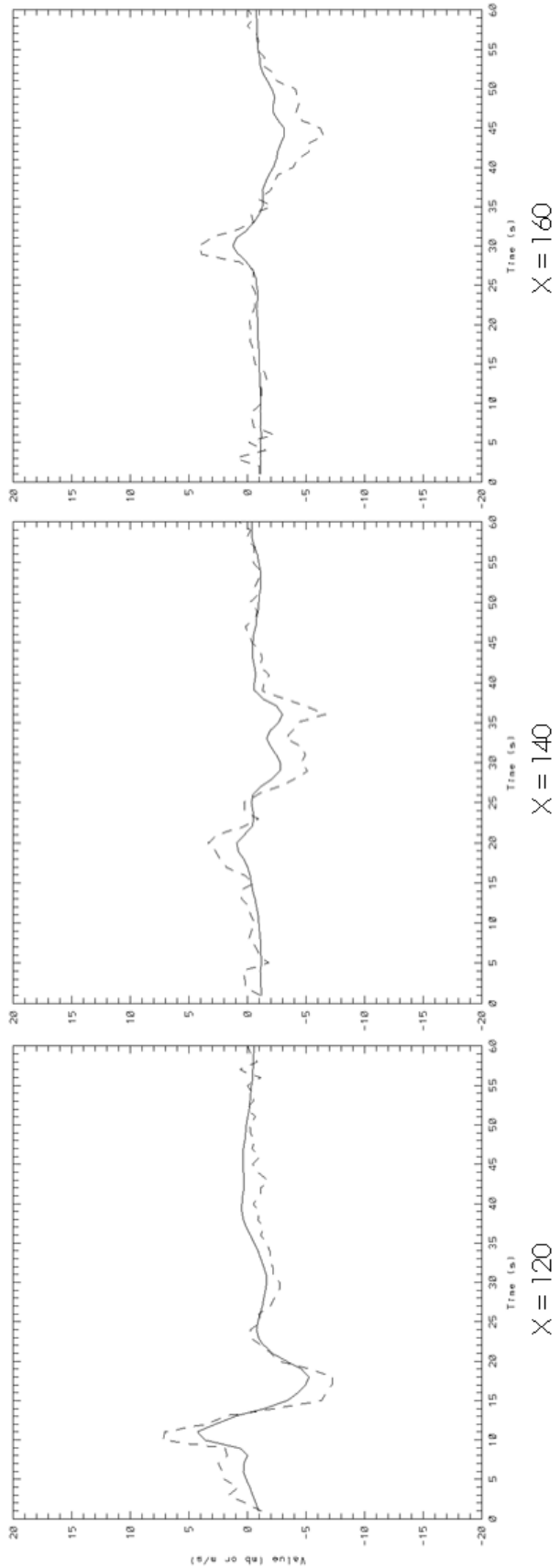

Figure 13. Timeline of U′ and P′ at points (120, 50), (140, 50), and (160, 50). P′ is multiplied by 5 to exaggerate the scale for comparison with U′. Wind is a solid line and pressure is a dotted line.

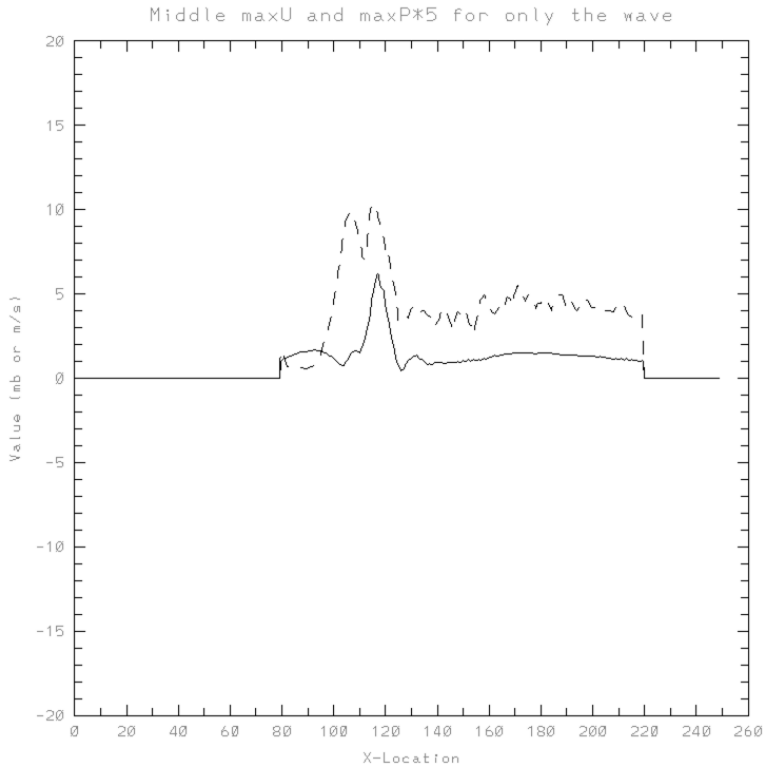

Figure 14. The maximum value at any time of U′ and P′ at all points along a line in the X direction through the domain Y center. P′ is multiplied by 5 to exaggerate the trend for comparison with U′. Only U′ and P′ values greater than 1m/s and 1mb are plotted.

The same patterns seen in Figure 13 are further exemplified by Figure 14, a comparison of maximum U′ and P′ at all points along a line in the x direction through the domain y center. In this figure, all pressure measurements are multiplied by 5 to allow the patterns of change to be more visible on the graph. As the cold thermal descends in the atmosphere, it impacts upon the stable layer, instigating changes in wind and pressure. At point 120, near the cold thermal impact point, a marked and correlated change in wind and pressure occurs with time. Beginning at 8 min, wind and pressure increase in value by 5.7 m/s and 2.1 mb, proceed to decrease at 12 min to 3.0 m/s and 1.3 mb, and return to a mean state at 23 min. These values are not scaled. For reference, point 120 in this simulation had the largest U′ and P′. A similar, albeit weaker pattern emerges at points

140 and 160 as the wave is progressing toward the east. Figure 14 shows the overall maximum increase in wind and pressure at each point over all time that occur throughout the simulation.

With MGWs, wind and pressure should change in a correlated manner, meaning that as U′ increases or decreases, there should be a proportional increase or decrease in P′. This is the case with the MGW presented within this simulation. As Figure 15 demonstrates, along the center line where the largest wave was observed, U′ and P′ perturbations > 1m/s and 1 mb respectfully changed in a correlated manner. Correlations are calculated from a time-series of U′ and P′ at each point in the model domain.

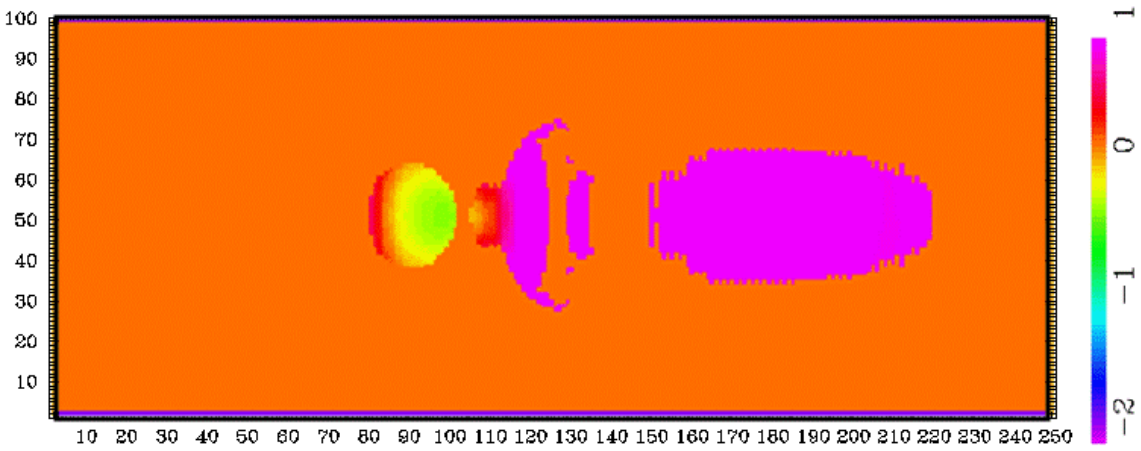

Figure 15. Correlation coefficient (r) on a surface plan view of the model domain. Correlations > 0.95 are shaded in purple. Large orange areas indicated regions where correlation was not calculated as U′ and P′ were less than 1m/s and 1mb.

4.3 Behavior of response variables

Diagrams illustrating the relationships between the response variables are presented in this section. Some generalizations emerge which are summarized briefly here before the details are presented. Γ_1 primarily affects the amplitude of wave perturbations. Smaller values favor larger perturbations while larger values favor smaller

perturbations. If both Γ_1 and ΔU increase, the observed behavior transitions from waves of elevation to waves of depression. The occurrence of heat bursts is more common when Γ_2 is neutral. Additionally, wave activity is much stronger when Γ_2 is neutral and when H_2 is larger, provided H_1 is large. When H_1 is shallow, wind speeds are much faster and the descending cold thermal obliterates the stable layer, producing a flow similar to a microburst. When H_1 is deep, however, wave activity appears in model solution as opposed to a microburst. Finally, with 0 m/s ΔU, the wave resembles a rock dropped in a pond appearing similar to an oscillating buoyancy wave. When ΔU is increased, there is a transition to a propagating solitary wave that resembles an ocean.

4.3.1 Simulations with 20 m/s ΔU with varying Γ_1 vs. H_1

In this set of simulations, the emphasis was on surface response to changes to the initial surface lapse rate and depth. In the first diagram (Figure 16), potential temperature and a comparison of surface U′ and P′ are portrayed at the extremities of the regime diagram domain. U′ is represented by a solid line and P′ is represented by a dotted line. The θ is shown in a vertical cross section at 20 minutes into the simulation near to the descending thermal impact point. U′ and P′ are time traces at point X = 120 km. These are only shown once for each set of regime diagrams to illustrate the differences in the wave behavior as the lapse rate and height change.

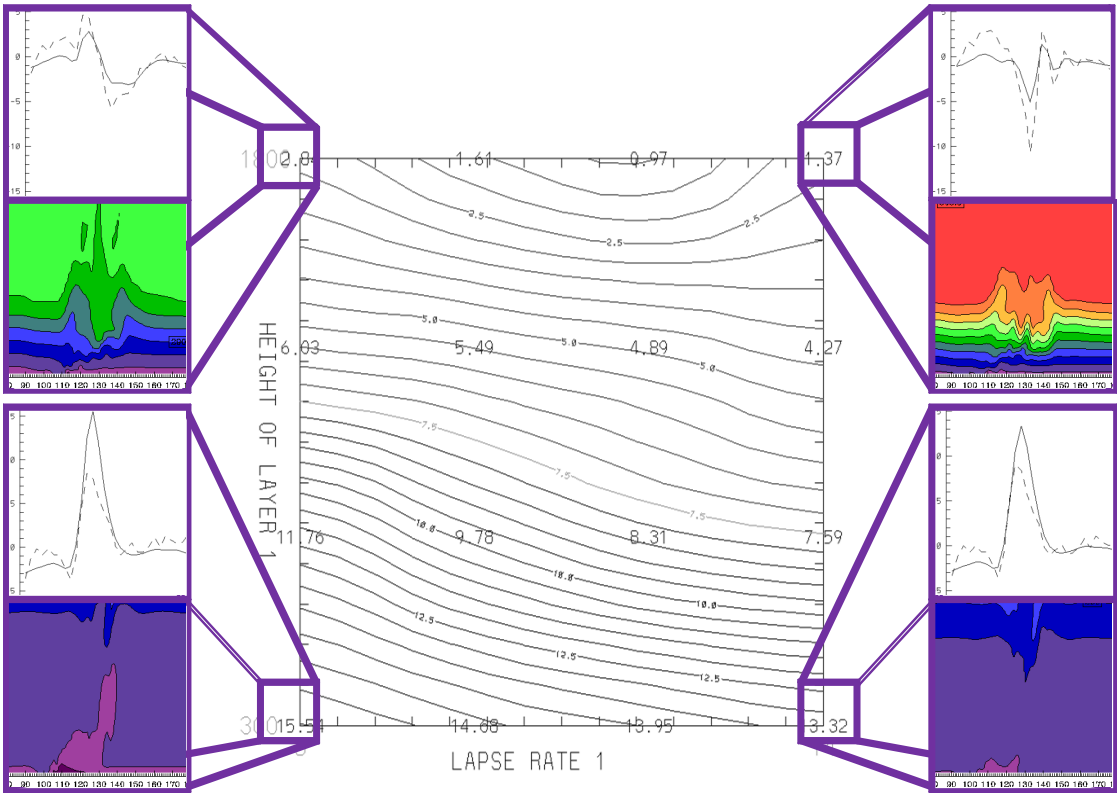

Figure 16. U′ and P′ at the extremities of the Regime Diagrams with conditions of ΔU = 20 m/s, Γ_1= 8-14 K/km, Γ_2=0 K/km, H_1=300-1800 m, and H_2=3000 m at point X=120 km.

Changes in U'_{max} are portrayed in Figure 17. U'_{max} ranges from 2.8 m/s to 15.5 m/s for Γ_1=8 K/km and from 1.3 m/s to 13.3 m/s for Γ_1=14 K/km as H_1 increases from 300 m to 1800 m. U'_{max} is less dependent upon changes in Γ_1, and more dependent upon changes in H_1. The largest U'_{max} occurred given the weakest and most shallow stable layers. This appears to be due to the ability of the thermal to pass entirely through the surface layer, impact upon the surface, and change the wind speed in a similar manner to a microburst while still retaining a correlated change in wind and pressure as seen with MGWs.

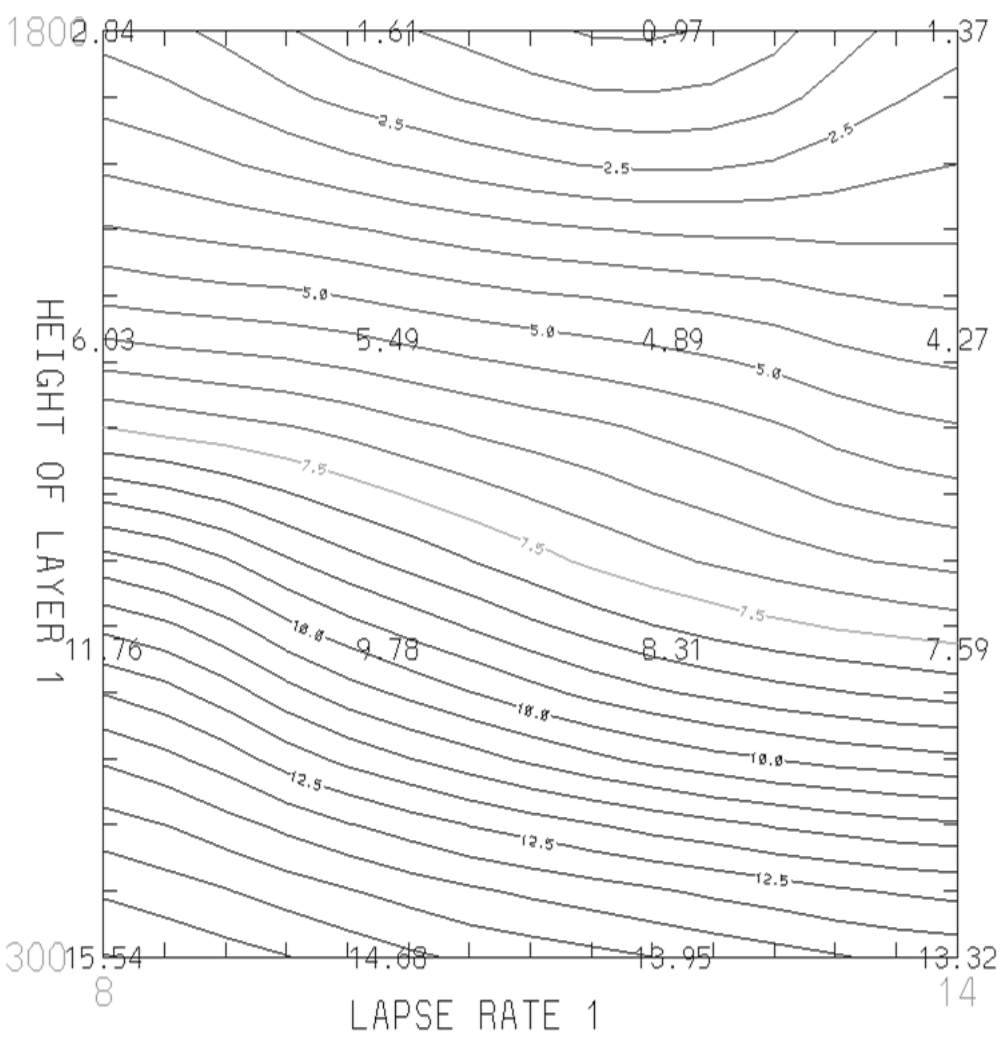

Figure 17. U'_{max} (contoured every 0.5 m/s) with conditions of ΔU = 20 m/s, Γ_1= 8-14 K/km, Γ_2=0 K/km, H_1=300-1800 m, and H_2=3000 m at point X=120 km.

The changes in U'_{min} are portrayed in Figure 18. U'_{min} ranges from -3.1 m/s to -2.9m/s for Γ_1=8 K/km and from -5.1 m/s to -2.8 m/s for Γ_1=14 K/km as H_1 decreases from 1800 m to 300 m. U'_{min} is less dependent upon changes that occur in Γ_1, and more dependent upon changes in H_1 as the largest perturbations occurred when H_1 increases in value. The largest (negative) U'min values occur for deeper (1300-1800m) surface layers and stronger lapse rates.

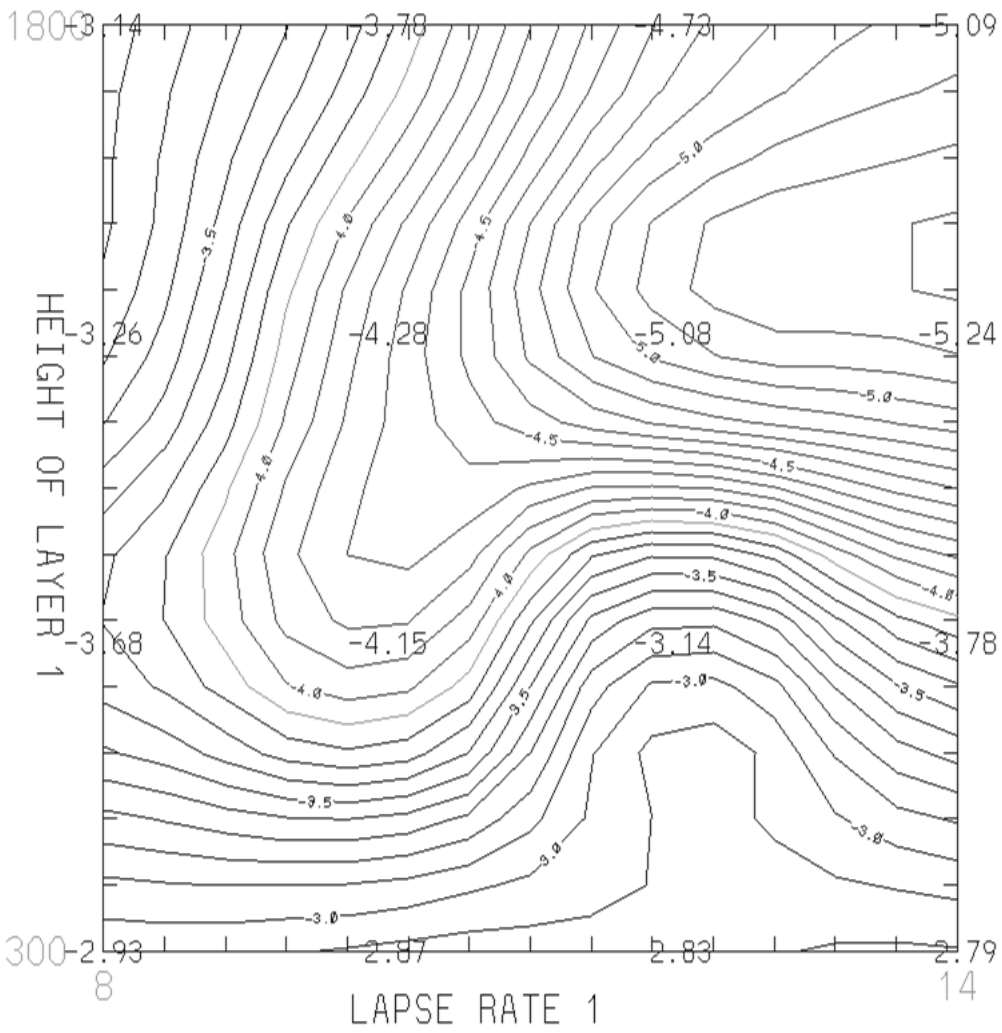

Figure 18. U'_{min} (contoured every 0.1 m/s) with conditions of ΔU = 20 m/s, Γ_1=8-14 K/km, Γ_2=0 K/km, H_1=300-1800 m, and H_2=3000 m at point X=120 km.

The changes in P'_{max} are portrayed in Figure 19. P'_{max} ranges from 0.9 mb to 1.9 mb for Γ_1=8 K/km and from 0.6 mb to 2.0 mb for Γ_1=14 K/km as H_1 decreases from 1800 m to 800 m. The largest value occurs when H_1 is 800 m. This appears, as with U'_{max}, to be due to the ability of the thermal to impact the surface in a similar manner to a microburst while still retaining a correlated change in wind and pressure as seen with MGWs. For values of H_1 less than or equal to 800m, as Γ_1 increases, pressure increases. For H_1 values greater than or equal to 1300 m, as Γ_1 increases, pressure decreases.

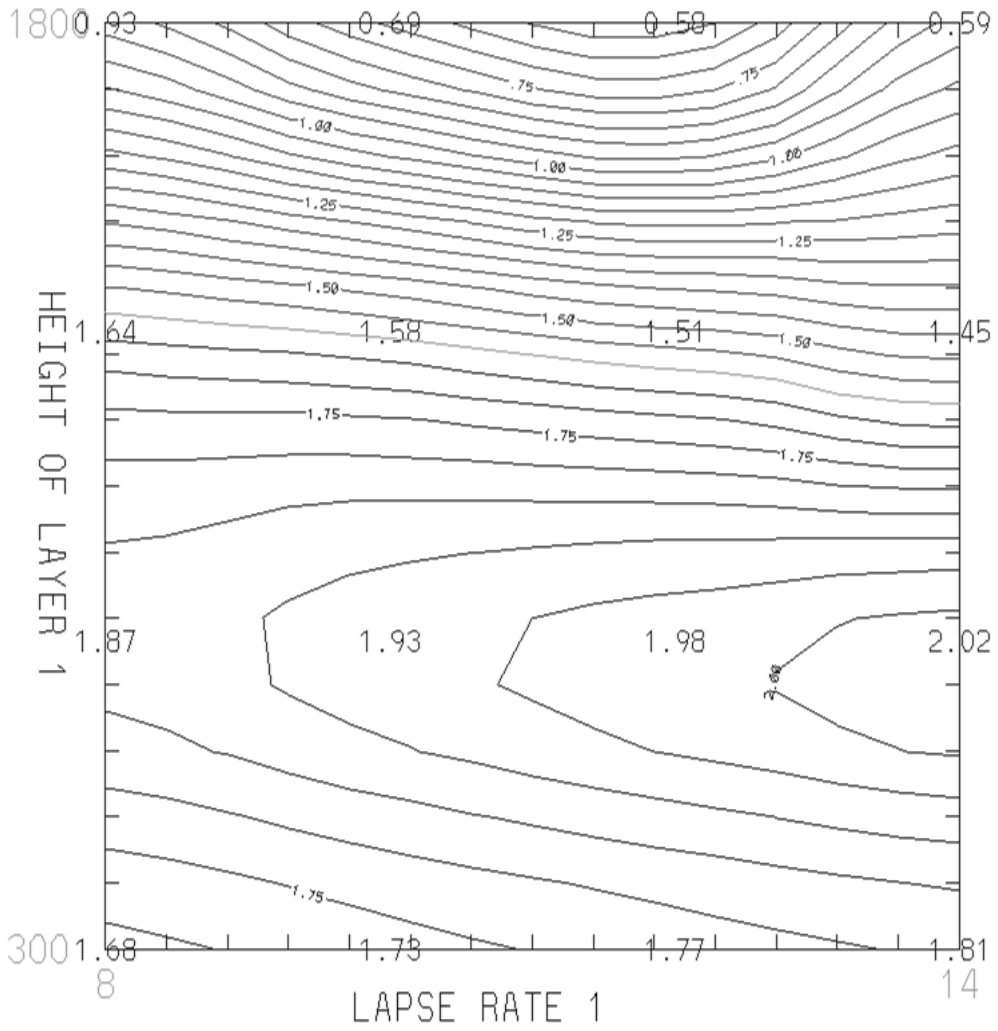

Figure 19. Regime Diagram for P'_{max} (contour interval 0.05 mb) with conditions of ΔU = 20m/s, Γ_1=8-14 K/km, Γ_2=0 K/km, H_1=300-1800m, and H_2=3000m at point X=120 km.

The changes in P'_{min} are portrayed in Figure 20. P'_{min} ranges from -1.2 mb to -0.7 mb for Γ_1=8 K/km and from -2.1 mb to -0.7 mb for Γ_1=14 K/km as H_1 decreases from 1800 m to 300 m. P'_{min} is less dependent upon changes in Γ_1 and more dependent upon changes in H_1. The largest negative perturbations occurred for the deepest H1 and strongest Γ_1.

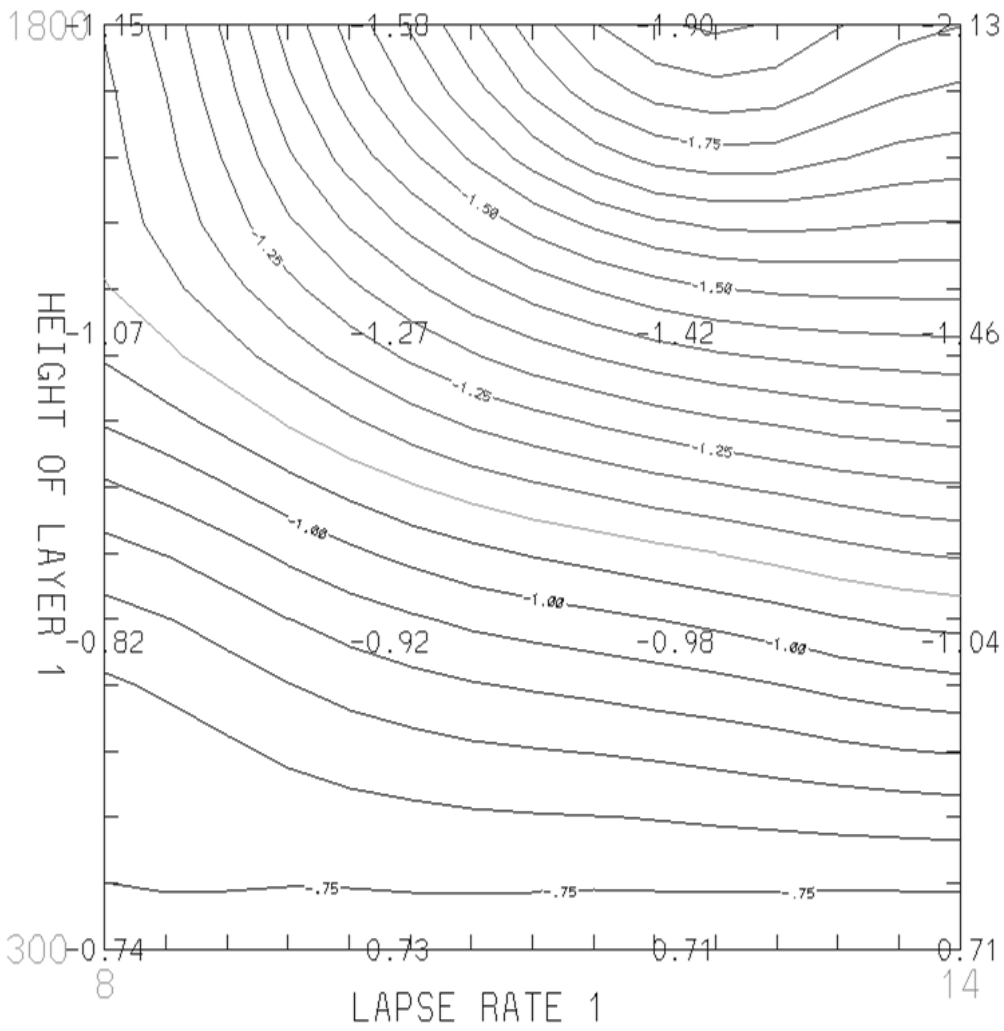

Figure 20. P'_{min} (contour interval 0.05 mb) with conditions of ΔU = 20 m/s, Γ_1=8-14 K/km, Γ_2=0 K/km, H_1=300-1800 m, and H_2=3000 m at point X=120 km.

The changes in T'_{max} are portrayed in Figure 21. T'_{max} ranges from -0.7 K to 1.8 K for Γ_1=8 K/km for H_1 between 300 m and 1800 m and from 0.3 K to 0.9 K for Γ_1=14 K/km as H_1 decreases from 1800 m–300 m. T'_{max} is less dependent upon changes in Γ_1, but more so upon H_1. There is an axis of maximum temperature perturbations for intermediate (800 m to 1300m) values of H_1, with the largest values occurring for the weakest stability values.

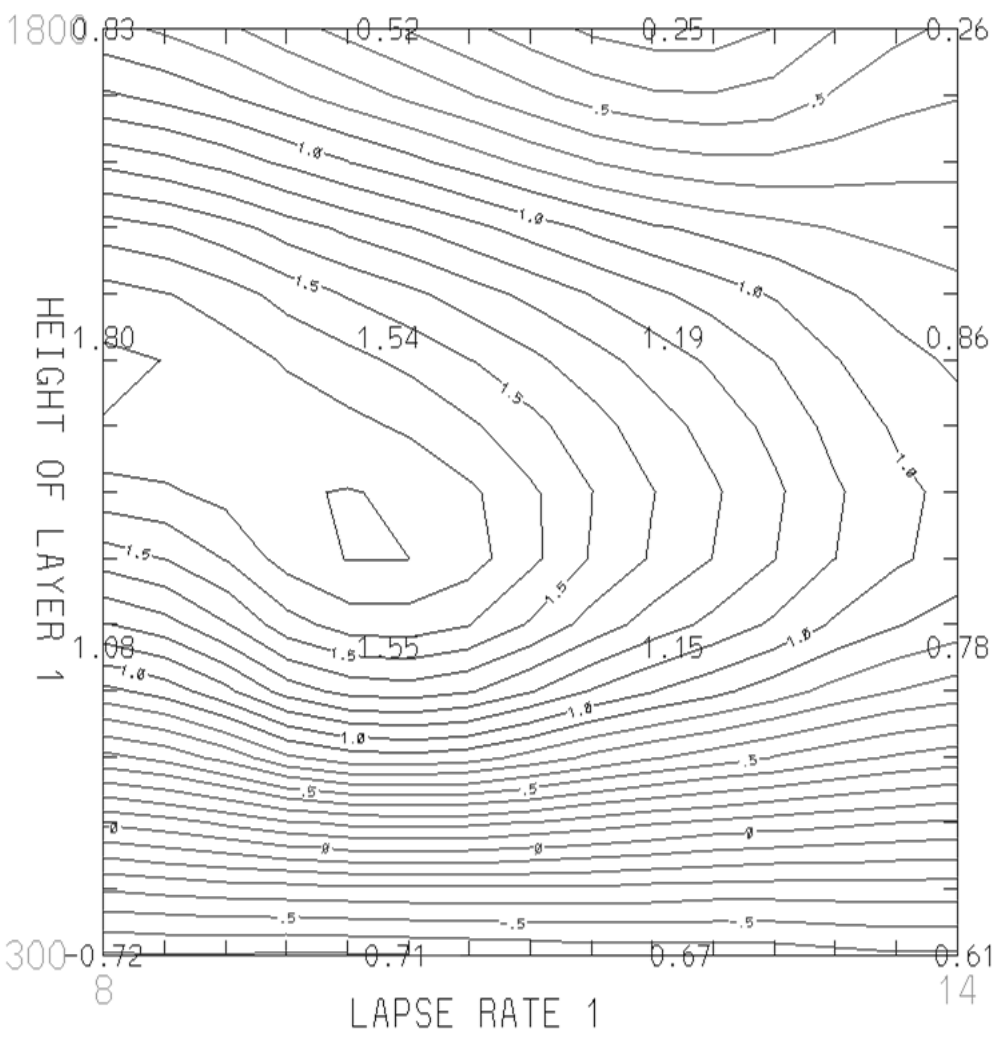

Figure 21. T'_{max} (contoured every 0.1 K) with conditions of ΔU = 20m/s, Γ_1=8-14 K/km, Γ_2=0 K/km, H_1=300-1800m, and H_2=3000m at point X=120 km.

The changes in T'_{min} are portrayed in Figure 22. T'_{min} ranges from -3.3 K to -0.2 K for Γ_1=8 K/km and from -2.0 K to -0.2 K for Γ_1=14 K/km as H_1 increases from 300 m–1800 m. T'_{min} is more dependent upon the value of H_1, as a shallower H_1 allows the thermal to cause a larger impact upon the surface. However, T'_{min} becomes less negative as Γ_1 increases in value.

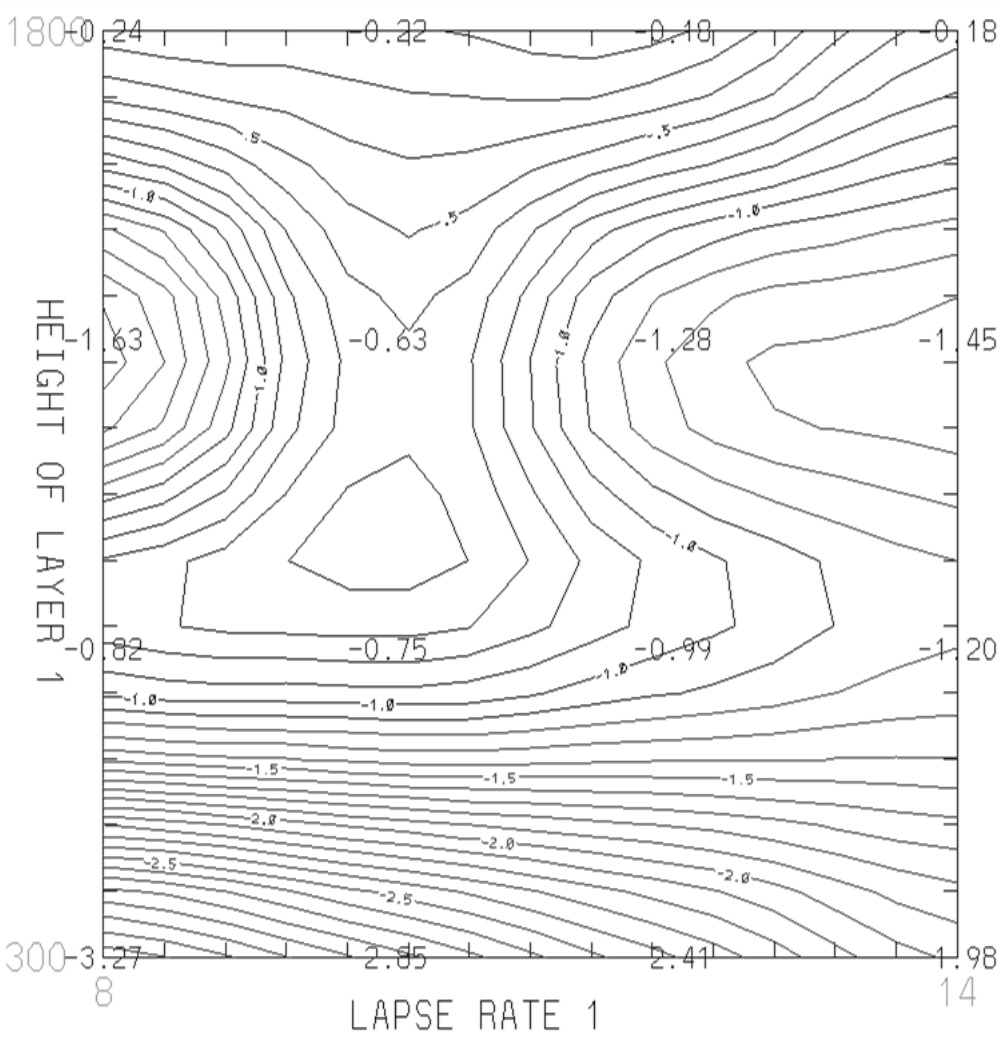

Figure 22. T'_{min} (contoured every 0.1 K) with conditions of ΔU = 20 m/s, Γ_1=8-14 K/km, Γ_2= 0 K/km, H_1=300-1800 m, and H_2=3000 m at point X=120 km.

The value of R was not highly dependent upon the changes in Γ_1 or H_1. All R values were very close in magnitude. This is evidenced by the model output in Figure 23.

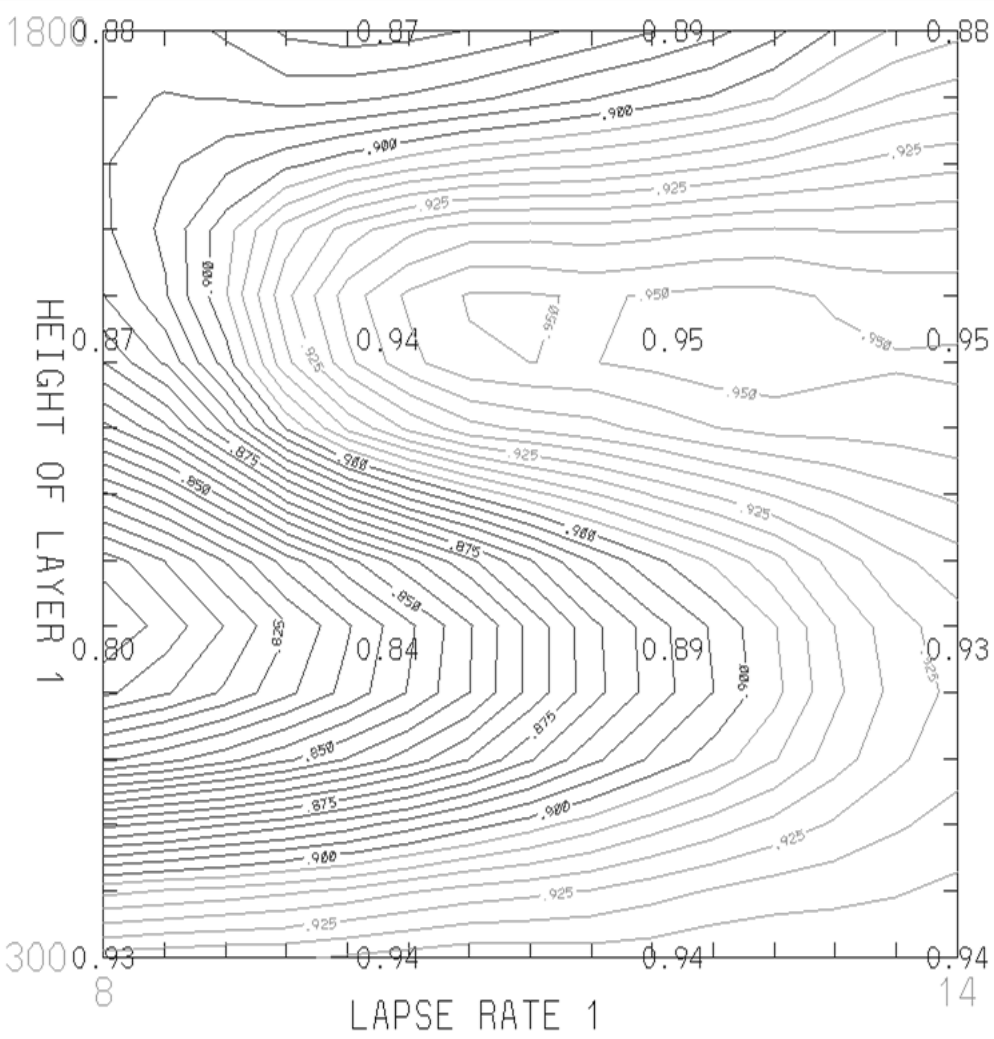

Figure 23. R (contoured every 0.001) with conditions of ΔU = 20 m/s, Γ_1=8-14 K/km, Γ_2=0 K/km, H_1=300-1800 m, and H_2=3000 m at point X=120 km.

Generally speaking, changes in U′ are more dependent upon changes in H_1 than on gamma1. Changes in P'_{min} are more dependent upon changes in H_1. The largest T′ are more dependent upon the value of H_1 and the most negative T' occurs with the most shallow H1. Correlation coefficient is neither highly dependent upon the changes in Γ_1 nor changes in H_1.

The model indicates a more traditional MGW response with a deep surface layer of 1300 – 1800 m. This is more apparent when the surface layer is very stable. However,

when the layer is shallower with a depth of 800 m, the behavior has characteristics of a traveling microburst, but with subtle surface heating at the surface on the order of 2 – 3 K. However, the behavior is still characteristic of a MGW based upon the results, such as the retention of the MGW characteristics of correlated changes in surface U′ and P′ in the vicinity of the initial cold thermal impact. Generally, this is described by a positively correlated change in U′ and P′ with a corresponding decrease in temperature. With a very shallow surface layer of 300 m, the behavior tends to have traveling microburst characteristics with a correlated change in U′ and P′ with a corresponding decrease in temperature. In the simulations shown in this section, there was no clear indication of heat burst activity.

4.3.2 Simulations with 20 m/s ΔU with varying Γ_2 vs. H_2

In this set of simulations, the emphasis was on surface response to the variance of the initial secondary level lapse rate and depth. In the first diagram shown below, potential temperature and a comparison of U′ and P′ are portrayed at the extremities of the regime diagram domain. Potential temperature is shown in a cross section at 20 minutes into the simulation near to the descending thermal impact point. U′ and P′ are a time trace at point X = 120 km. These are only shown once to illustrate the differences in the wave behavior as the second-layer lapse rate and height change.

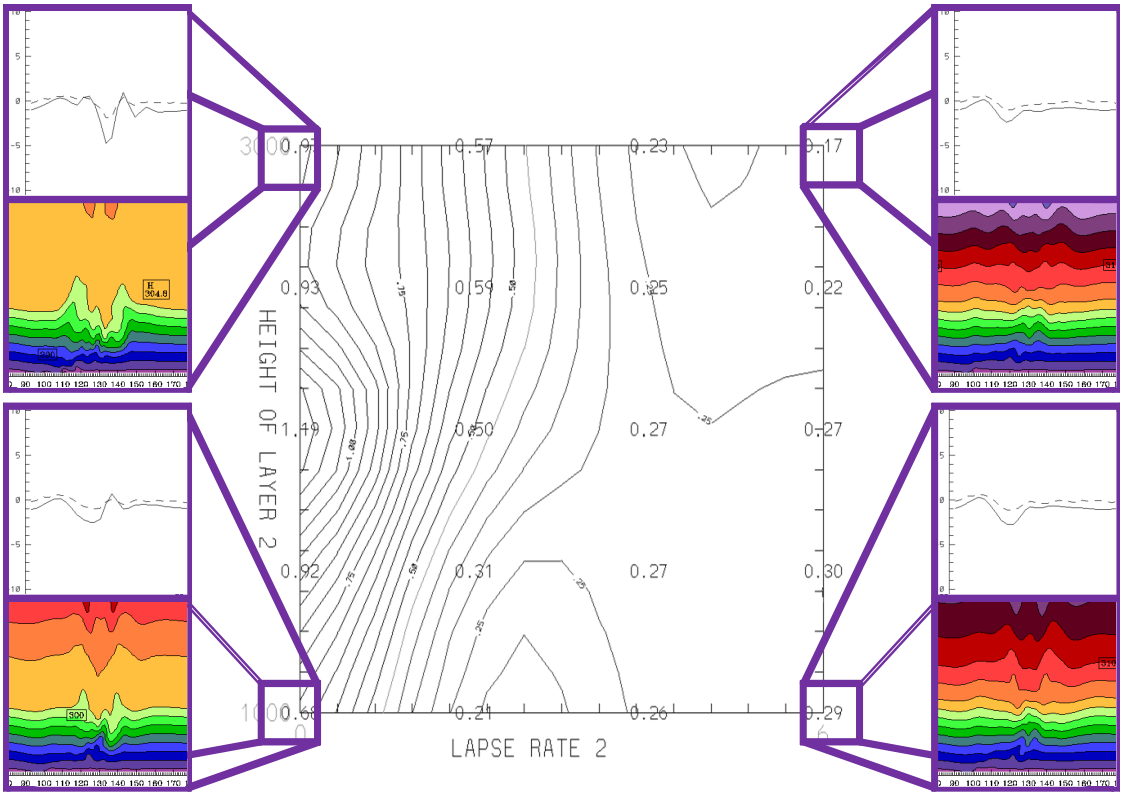

Figure 24. U′ and P′ at the extremities of the Regime Diagrams with conditions of ΔU = 20m/s, Γ_1=12 K/km, Γ_2=0-6 K/km, H_1=1800 m, and H_2=1000-3000 m at point X=120 km.

As is shown in Figure 25, U'_{max} ranges from 0.7 m/s to 1.5m/s for Γ_2=0 K/km among the range of H_2 between 1000 m and 3000 m, while showing little variation for non-neutral conditions, ranging from 0.2m/s to 0.3 m/s for Γ_2=6 K/km as H_2 increases from 1000 m to 3000 m. The largest U'_{max} occurs for a neutral layer with a depth of 2000m. U'_{max} is more dependent upon changes in Γ_2, and the largest perturbations occurred when Γ_2 was 0 K/km.

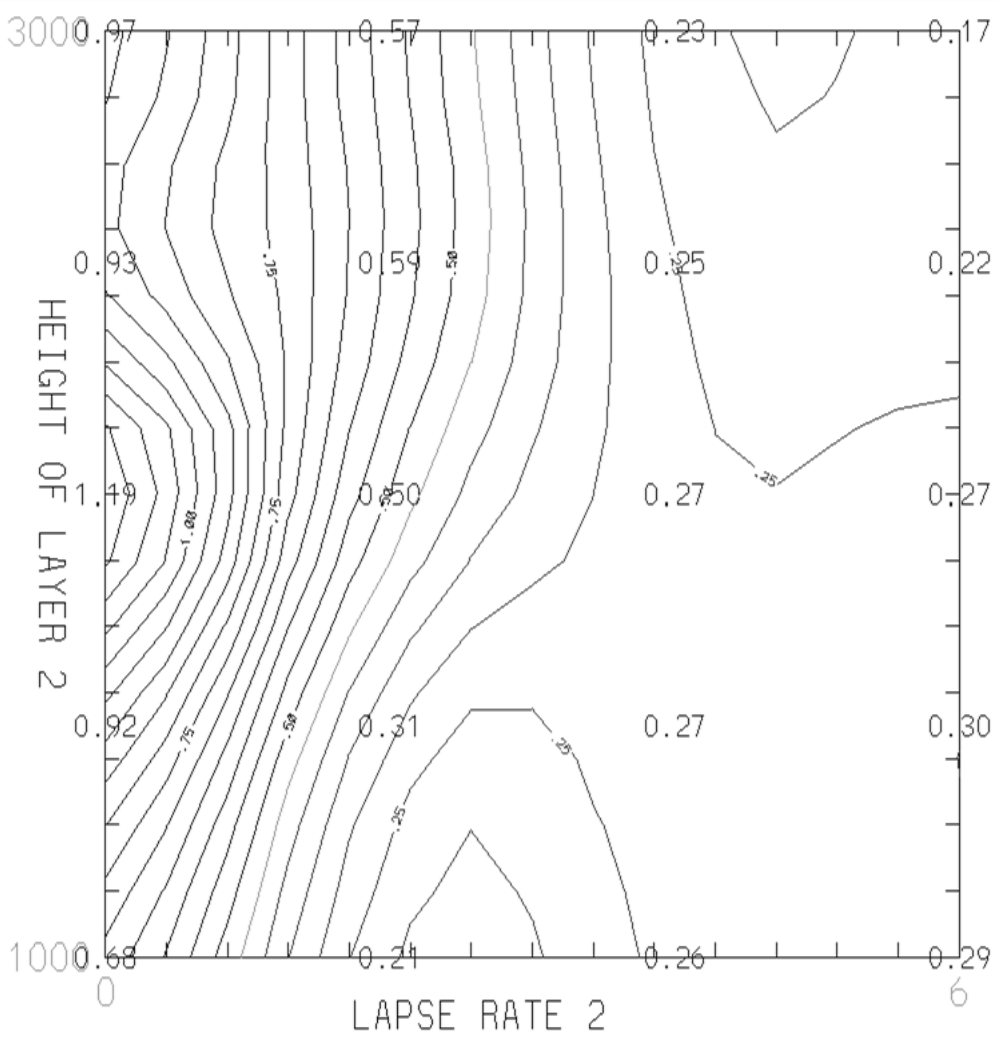

Figure 25. U'_{max} (contoured every 0.05 mb) with conditions of ΔU = 20m/s, Γ_1=12 K/km, Γ_2=0-6 K/km, H_1=1800 m, and H_2=1000-3000 m at point X=120 km.

As is shown in Figure 26, U'_{min} ranges from -4.7 m/s to -2.5 m/s for Γ_2=0 K/km as H_2 decreases from 3000 m–1000 m, and also ranges from -2.8 m/s to -2.4 m/s for Γ_2=6 K/km as H_2 increases from 1000 m–3000 m. U'_{min} is inversely dependent upon changes in Γ_2. For Γ_2 values less than or equal to 2 K/km, as H_2 increases, U'_{min} increases, For Γ_2 values greater than or equal to 4 K/km, as H_2 increases, U'_{min} decreases. The largest negative U'_{min} occurs with a deep neutral layer as this allows for the thermal to fall uninhibited over time and impact the surface layer with the most force possible. The

change tends to be more negative than positive as the surface layer tends to form a depression with a minimal positive increase. With a non-neutral layer, the thermal becomes less buoyant over time, causing a decrease in the force with which it impacts the surface layer. Therefore, the impacts are much less dramatic than for the neutral second layer.

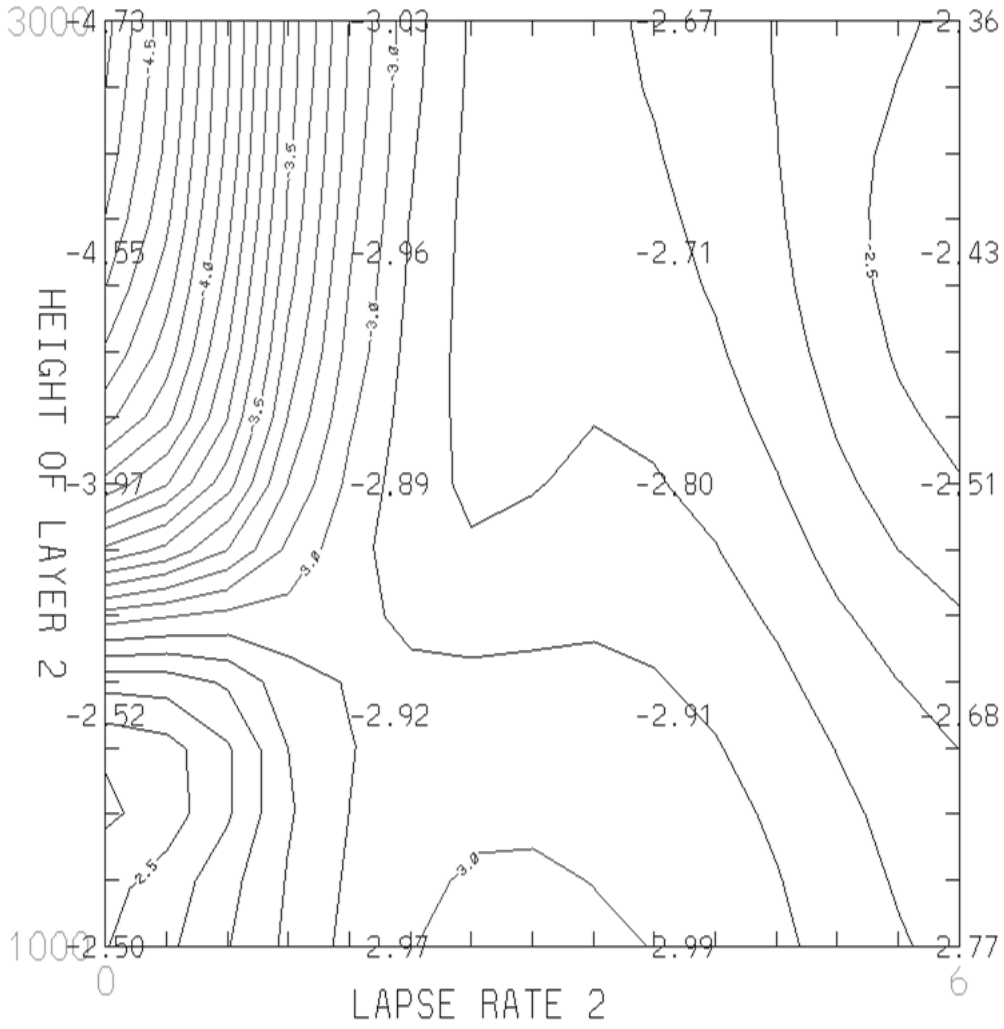

Figure 26. U'_{min} (contoured every 0.1 mb) with conditions of ΔU = 20 m/s, Γ_1=12 K/km, Γ_2=0-6 K/km, H_1=1800 m, and H_2=1000-3000 m at point X=120 km.

Figure 27 portrays the behavior of P'_{max}. The values for P'_{max} range from 0.5 mb to 0.6 mb for a Γ_2 value of 0 K/km. The largest P'_{max} for this neutral case occurred when H_2 was 1000 m and 3000 m, and the smallest P'_{max} occurred when H_2 was 2000 m. P'_{max} ranged from 0.64 mb to 0.67 mb for a Γ_2 of 6 K/km. The largest P'_{max} for this most stable case occurred when H_2 was 1500 m and 2000 m and the smallest P'_{max} occurred when H_2 was 3000 m. Generally speaking, P'_{max} tend to increase as Γ_2 increases in value at all heights.

Figure 28 portrays P'_{min}. It ranges from -1.9 mb to -1.0 mb for Γ_2 = 0 K/km as H_2 decreases from 3000 m to 1000 m. P'_{min} ranged from -1.2 mb to -1.0 mb for Γ_2 = 6 K/km. The most negative P'_{min} occurred when H_2 was 3000 m and the least negative P'_{min} occurred when H_2 was 1000 m with Γ_2 = 0K/km and H_2 was 3000m with Γ_2 = 6K/km. For Γ_2 values less than or equal to 2 K/km, as H_2 increases, P'_{min} becomes more negative. However, for Γ_2 values greater than or equal to 4 K/km, as H_2 increases, P'_{min} less negative. The subsidence following the sinking thermal in the model is significant as it leads to hydrostatic pressure falls.

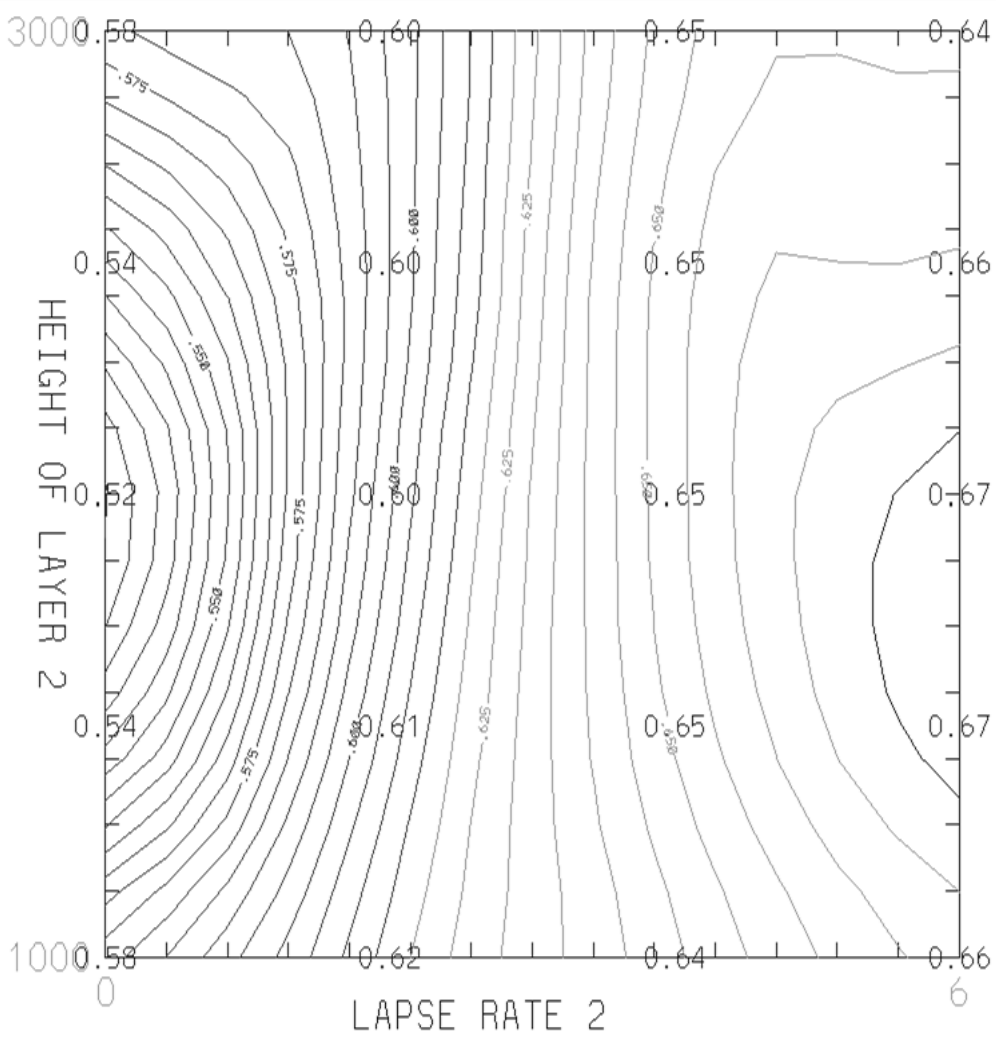

Figure 27. P'_{max} (contoured every 0.005 mb) with conditions of ΔU = 20 m/s, Γ_1=12 K/km, Γ_2=0-6 K/km, H_1=1800 m, and H_2=1000-3000 m at point X=120 km.

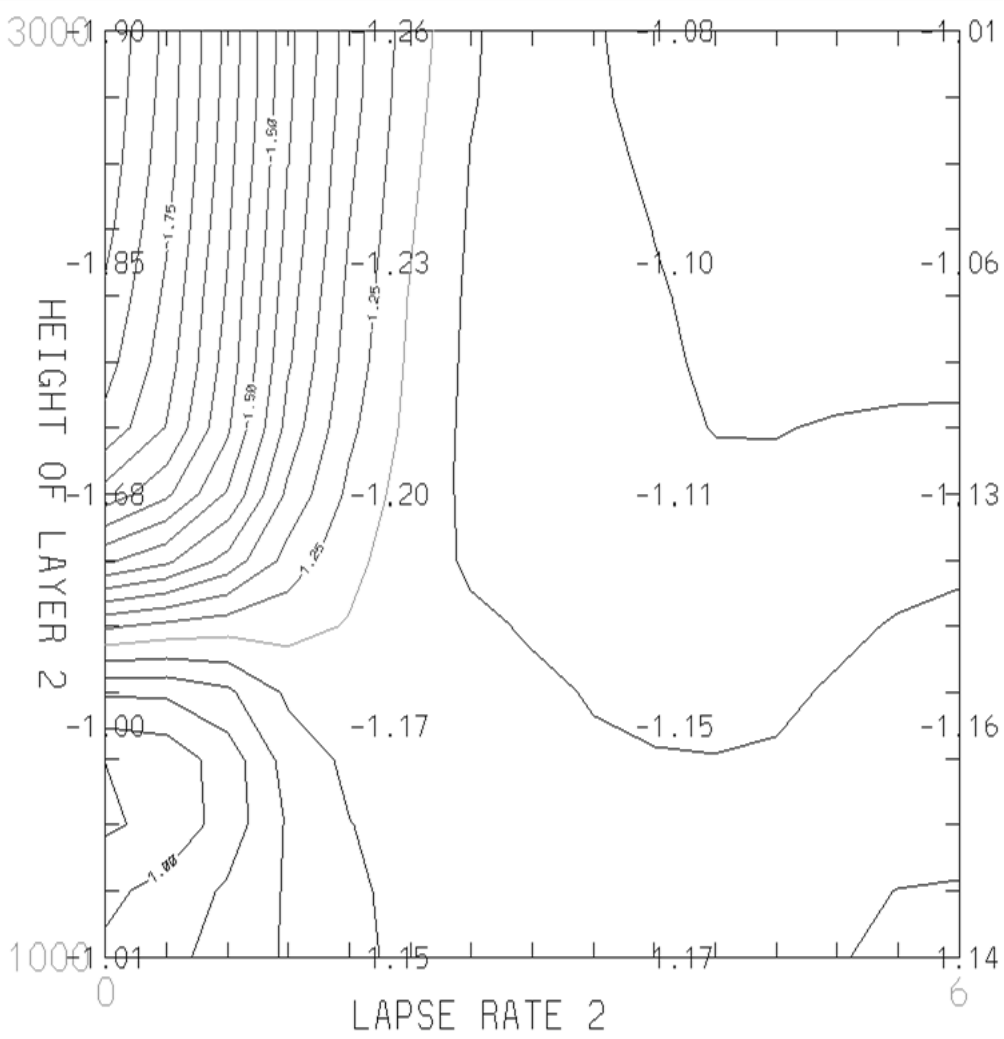

Figure 28. P'_{min} (contoured every 0.05 m/b) with conditions of ΔU = 20 m/s, Γ_1=12 K/km, Γ_2=0-6 K/km, H_1=1800 m, and H_2=1000-3000 m at point X=120 km.

As depicted in Figure 29, T'_{max} ranges from 0.1 K to 0.4 K. The maximum T'_{max} for this neutral second layer occurs when H_2 is 2000 m. T'_{max} ranges from 0.05 K to 0.11 K for Γ_2=6 K/km as H_2 decreases from 3000 m to 1000 m. T'_{max} is differentially dependent upon Γ_2. When Γ_2 is 0 K/km, higher temperature perturbations occur with mid-range values of H_2. For a Γ_2 values of 2 K/km, higher T'_{max} values occur at the extremities of H_2. For Γ_2 values greater than or equal to 4 K/km, as H_2 increases, T'_{max}

decreases. However, the range of these values is minimal when compared to the spread depicted with Γ_2 = 0K/km.

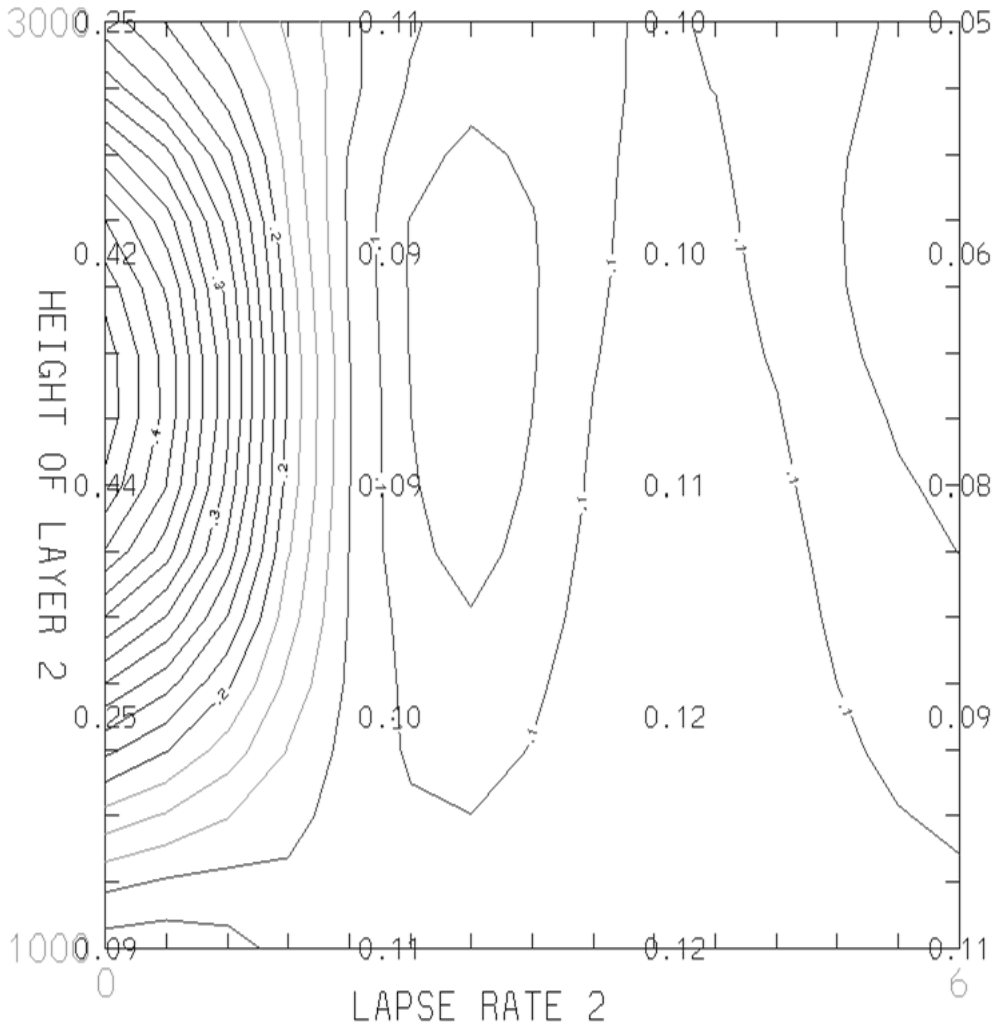

Figure 29. T'_{max} (contoured every 0.05 K) with conditions of ΔU = 20 m/s, Γ_1=12 K/km, Γ_2=0-6 K/km, H_1=1800 m, and H_2=1000-3000 m at point X=120 km.

As Figure 30 depicts, T'_{min} range from -0.2 K to -0.1 K for Γ_2=0 K/km and from -0.4 K to -0.2 K for Γ_2=6 K/km as H_2 decreases from 3000 m to 1000 m. The range of surface values tends to be minimal, but the overall most negative T'_{min} occurs with the deepest and most stable layer. T'_{min} is differentially dependent upon Γ_2. When Γ_2 is 0

K/km, 2 K/km, and 6 K/km, larger T'_{min} occur with lower values of H_2. For a Γ_2 value of 4 K/km, the maximum negative T'_{min} occurs with an H_2 value of 2500 m, with a general trend of increasing as H_2 increases.

Figure 31 depicts the value of the correlation coefficient. On the whole, pressure-wind correlations are high. The highest correlation observed within the model data occurs for the deepest neutral layer case, with a value of 0.89. With the neutral second layer, lower correlation values are found for the shallowest layers investigated. For Γ_2 values less than or equal to 2 K/km, as H_2 increases, R increases. For H_2 greater than or equal to 4 K/km, as H_2 increases, R decreases.

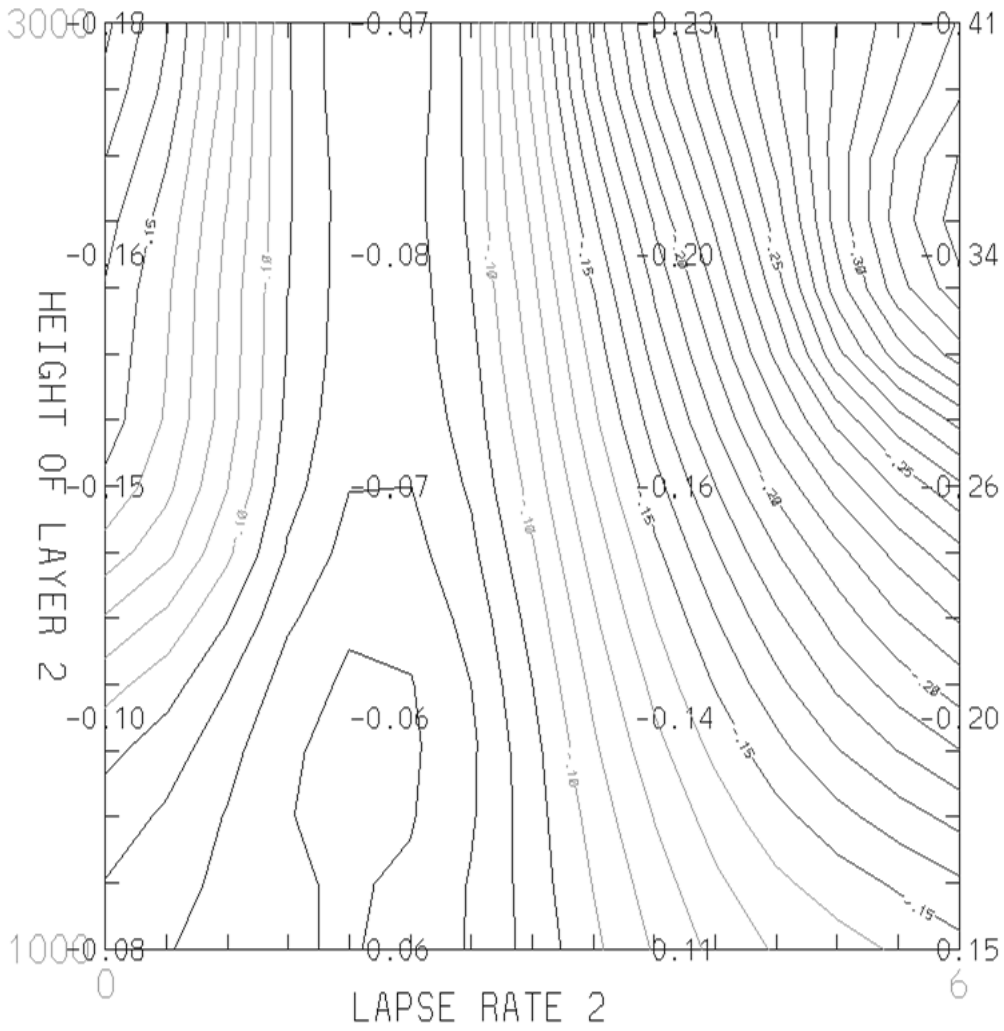

Figure 30. T'_{min} (contoured every 0.1 K) with conditions of ΔU = 20 m/s, Γ_1=12 K/km, Γ_2=0-6 K/km, H_1=1800 m, and H_2=1000-3000 m at point X=120 km.

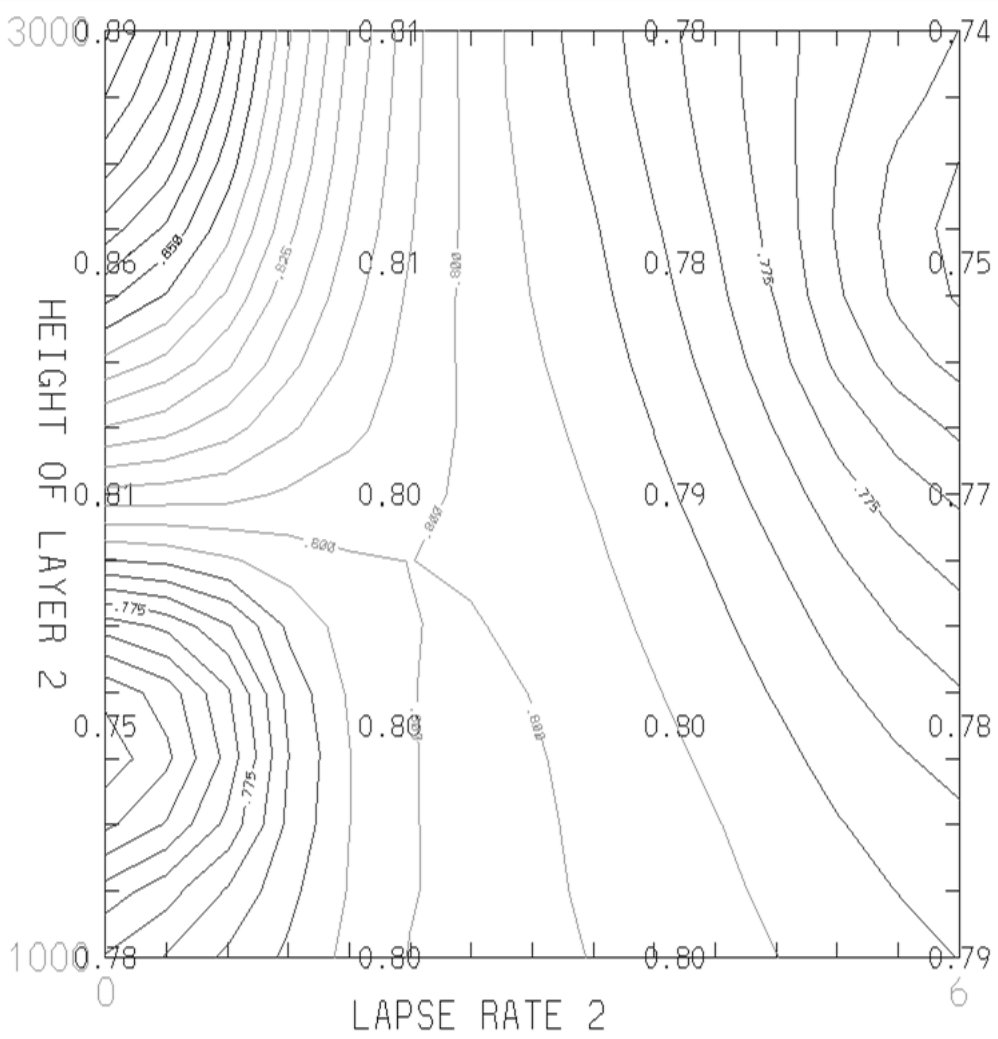

Figure 31. R (contoured every 0.005) with conditions of ΔU = 20 m/s, Γ_1=12 K/km, Γ_2=0-6 K/km, H_1=1800 m, and H_2=1000-3000 m at point X=120 km.

Looking generally at this subset of experiments, U'_{max} is more dependent upon changes in Γ_2 while U'_{min} is inversely dependent upon both Γ_2. The values of P'_{max} tend to increase as Γ_2 increases while P'_{min} is dependent upon Γ_2 changes. The variance of T' within the model is differentially dependent upon both Γ_2 and H_2. R is variably dependent upon the changes in Γ_2 and H_2.

The behavior of the model produces a more traditional MGW response with a deep second layer. This happens regardless of the lapse rate, but is more apparent when

the lapse rate is neutral as this allows for the cold thermal to fall uninhibited through the atmosphere. As the lapse rate is increased, the MGWs become weaker and more damped in terms of their variation in U′ and P′. The largest U'_{max} occurs with larger H_2. The largest correlation and the most negative values of U'_{min}, P'_{min} and T'_{min} occur with the deepest H_2 when coupled with neutral conditions. There was no clear indication of heat burst or microburst activity in these simulations.

4.3.3 Simulations with varying Γ_1 vs. ΔU

In this set of simulations, the lowest-layer stability and vertical shear were varied to examine the surface response. In the first diagram, potential temperature and a comparison of U′ and P′ are portrayed at the extremities of the regime diagram domain. Potential temperature is shown in a cross section at 20 minutes into the simulation near to the cold thermal impact point. U′ and P′ are a time trace at the points of X=110 km for ΔU = 0 m/s, X=120 km for ΔU = 10 m/s, and X=155 km for ΔU = 20 m/s and 30 m/s. These points were chosen to represent the effect of impact downwind of the point of origin, but still within the region of wave influence. The cross sections and time series are only shown once for this simulation set to illustrate the difference in the wave behavior as the lapse rate and height change.

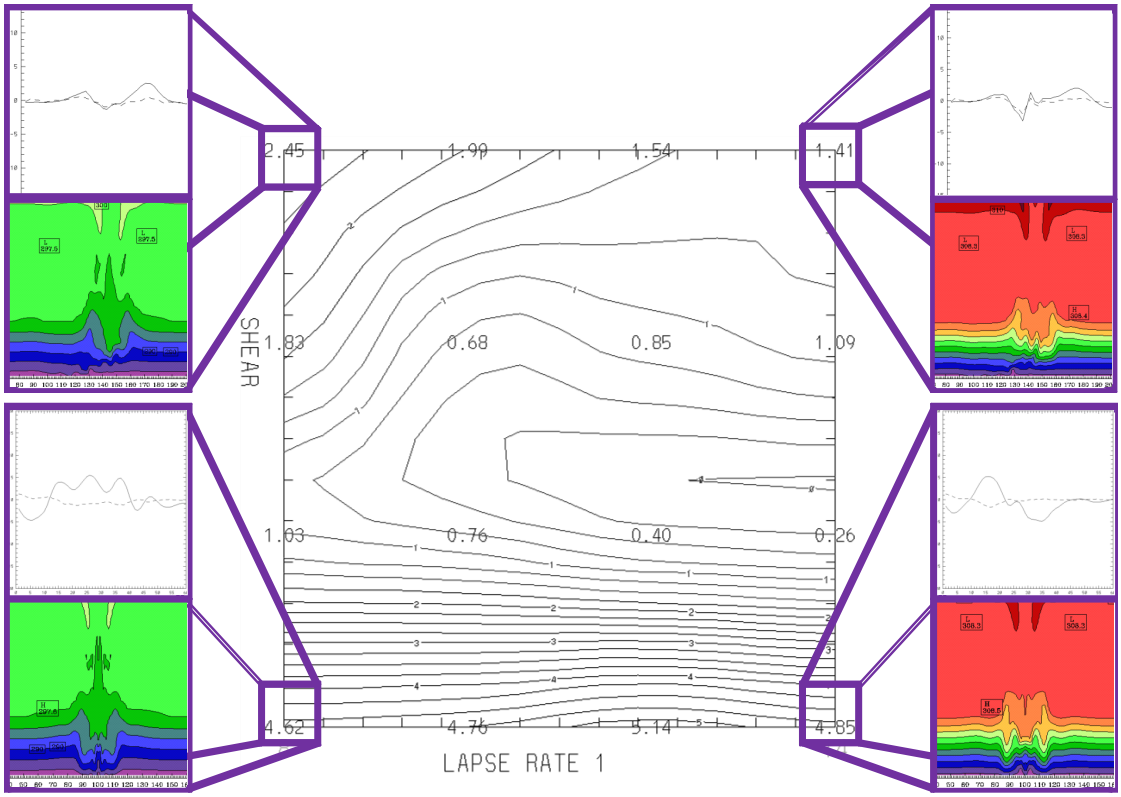

Figure 32. U′ and P′ at the extremities of the Regime Diagrams for ΔU = 0-30 m/s, Γ_1=8-14 K/km, Γ_2=0 K/km, H_1=1800 m, and H_2=3000 m. Model output is at point X=110 km for ΔU 0 m/s, X=120 km for ΔU 10 m/s, X=155 km for ΔU 20 m/s and 30 m/s.

In Figure 33, U'_{max} ranges from 1.0 m/s to 4.6 m/s for a Γ_1 of 8 K/km, and from 0.3 m/s to 4.9 m/s for a Γ_1 of 14 K/km. ΔU at 0 m/s produces the largest perturbations, after which U'_{max} generally increases with increasing shear from ΔU 10 m/s to 30 m/s. The maximum U'_{max} was 5.1 m/s with a Γ_1 of 12 K/km and ΔU of 0 m/s. As such, ΔU tends to affect U'_{max} the most as opposed to the surface layer stability.

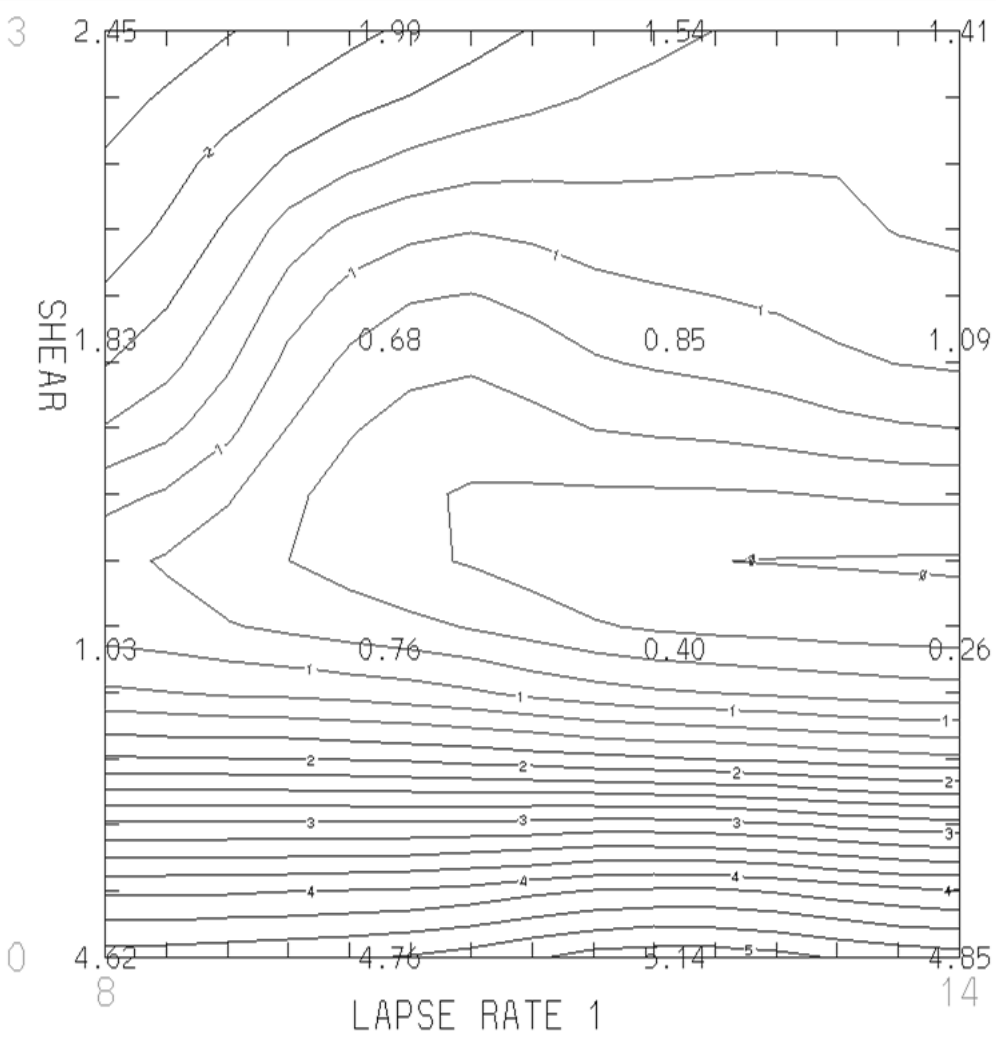

Figure 33. U'_{max} (contoured every 0.25 m/s) for ΔU = 0-30 m/s, Γ_1=8-14 K/km, Γ_2=0 K/km, H_1=1800 m, and H_2=3000 m. Model output is at point X=110 km for ΔU 0 m/s, X=120 km for ΔU 10 m/s, X=155 km for ΔU 20 m/s and 30 m/s.

In Figure 34, U'_{min} ranges from -5.5 m/s to -1.7 m/s for a Γ_1 of 8 K/km and from -5.3 m/s to -2.1 m/s for a Γ_1 of 14 K/km as ΔU increases from 0 m/s to 30 m/s. In the model, ΔU is the variable that most directly affects the U'_{min}.

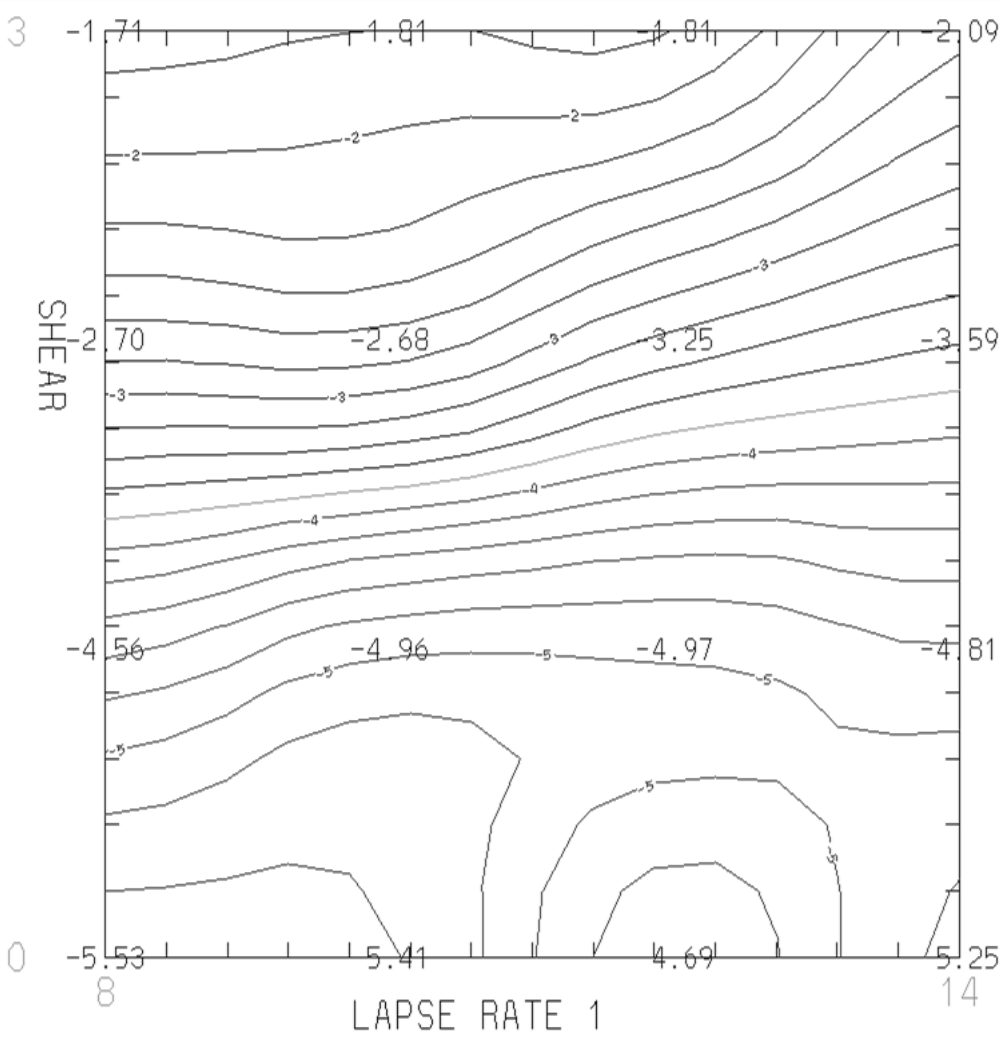

Figure 34. U'_{min} (contoured every 0.25 m/s) for ΔU = 0-30 m/s, Γ_1=8-14 K/km, Γ_2=0 K/km, H_1=180 0m, and H_2=3000 m. Model output is at point X=110 km for ΔU 0 m/s, X=120 km for ΔU 10 m/s, X=155 km for ΔU 20 m/s and 30 m/s.

In Figure 35, values for P'_{max} range from 0.6 mb to 1.3 mb for a Γ_1 of 8 K/km and from 0.6 mb to 1.3 mb for a Γ_1 of 14 K/km as ΔU decreases from 30 m/s to 0 m/s. The largest P'_{max} was 1.4 mb with a Γ_1 of 12 K/km and ΔU of 0 m/s. In the model, the largest P'_{max} ultimately occurred with 0 m/s ΔU.

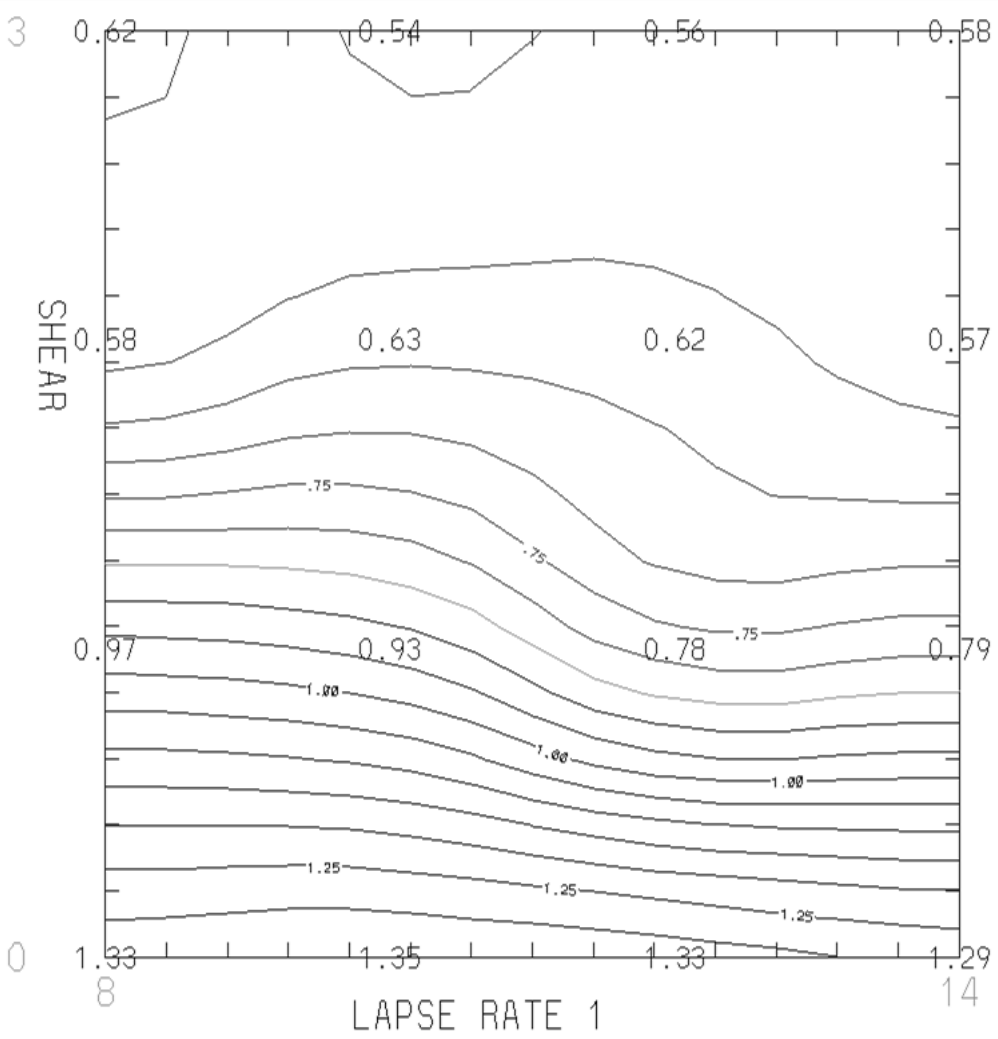

Figure 35. P'_{max} (contoured every 0.05 mb) for ΔU = 0-30 m/s, Γ_1=8-14 K/km, Γ_2=0 K/km, H_1=1800 m, and H_2=3000 m. Model output is at point X=110 km for ΔU 0 m/s, X=120 km for ΔU 10 m/s, X=155 km for ΔU 20 m/s and 30 m/s.

In Figure 36, values for P'_{min} ranges from -1.3 mb to -1.1 mb for Γ_1=8 K/km, with the most negative P'_{min} occurring with a ΔU of 10 m/s. At a Γ_1 of 14 K/km as ΔU decreases from 30 m/s to 0 m/s, P' ranges from -1.4 mb to -1.6 mb. P'_{min} tends to increase (negatively) as Γ_1 increases. However, P'_{min} is differentially dependent on ΔU. For $\Gamma_1 \leq$ 12 K/km, the largest negative P'_{min} occurs with a ΔU of 10 m/s. For Γ_1 = 14 K/km, the largest P'_{min} occurs with ΔU 20 m/s.

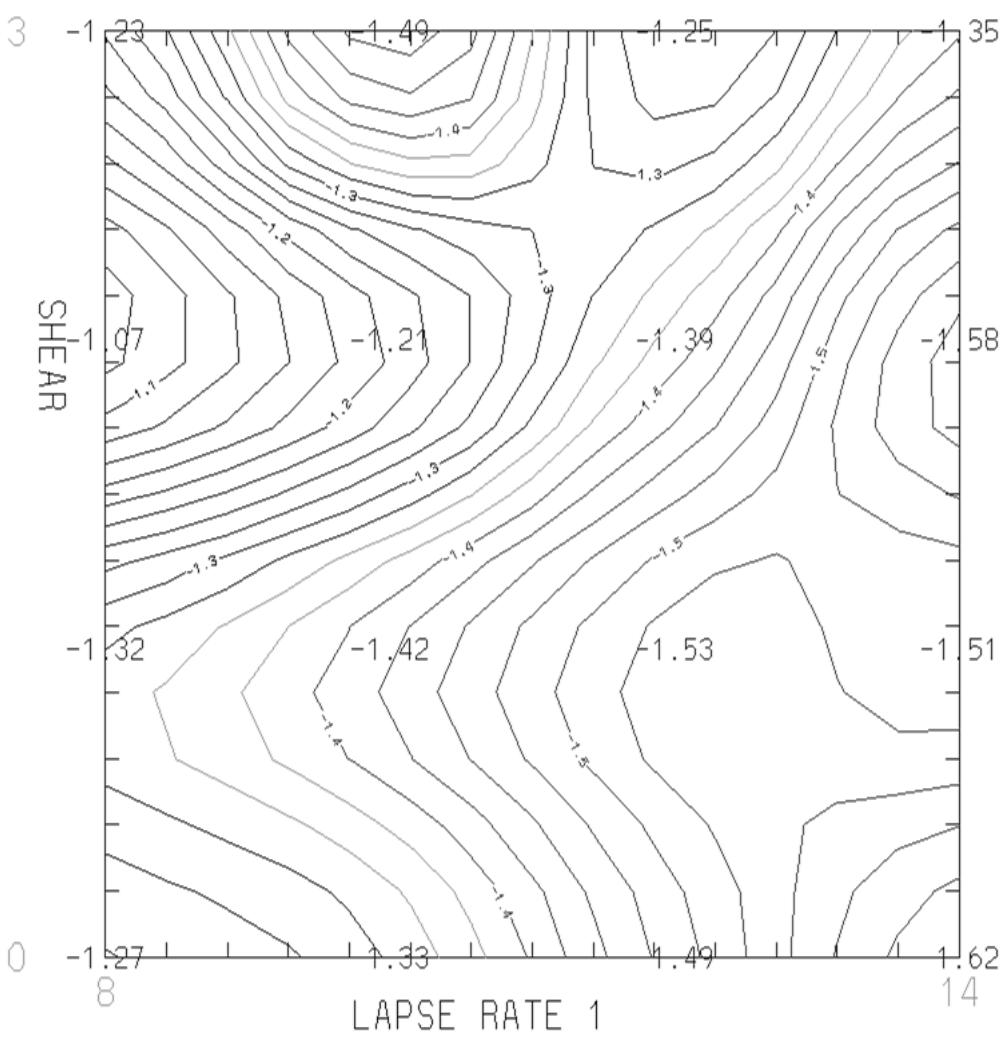

Figure 36. P'_{min} (contoured every 0.05 mb) for ΔU = 0-30 m/s, Γ_1=8-14 K/km, Γ_2=0 K/km, H_1=1800 m, and H_2=3000 m. Model output is at point X=110 km for ΔU 0 m/s, X=120 km for ΔU 10 m/s, X=155 km for ΔU 20 m/s and 30 m/s.

The values of the T'_{max} are portrayed in Figure 37. T'_{max} ranges from 0.1 K to 1.9 K for a Γ_1 of 8 K/km, and ranges from 0.1 K to 0.8 K for a Γ_1 of 14 K/km. The minimum T'_{max} occurred with ΔU of 20 m/s. The maximum T'_{max} is most dependent upon ΔU as perturbations generally increase as ΔU decreases. The maximum T'_{max} occurs for no shear and the weakest stability of the surface-based layer. Additionally, there is a clear demarcation in T'_{max} when ΔU is introduced into the model.

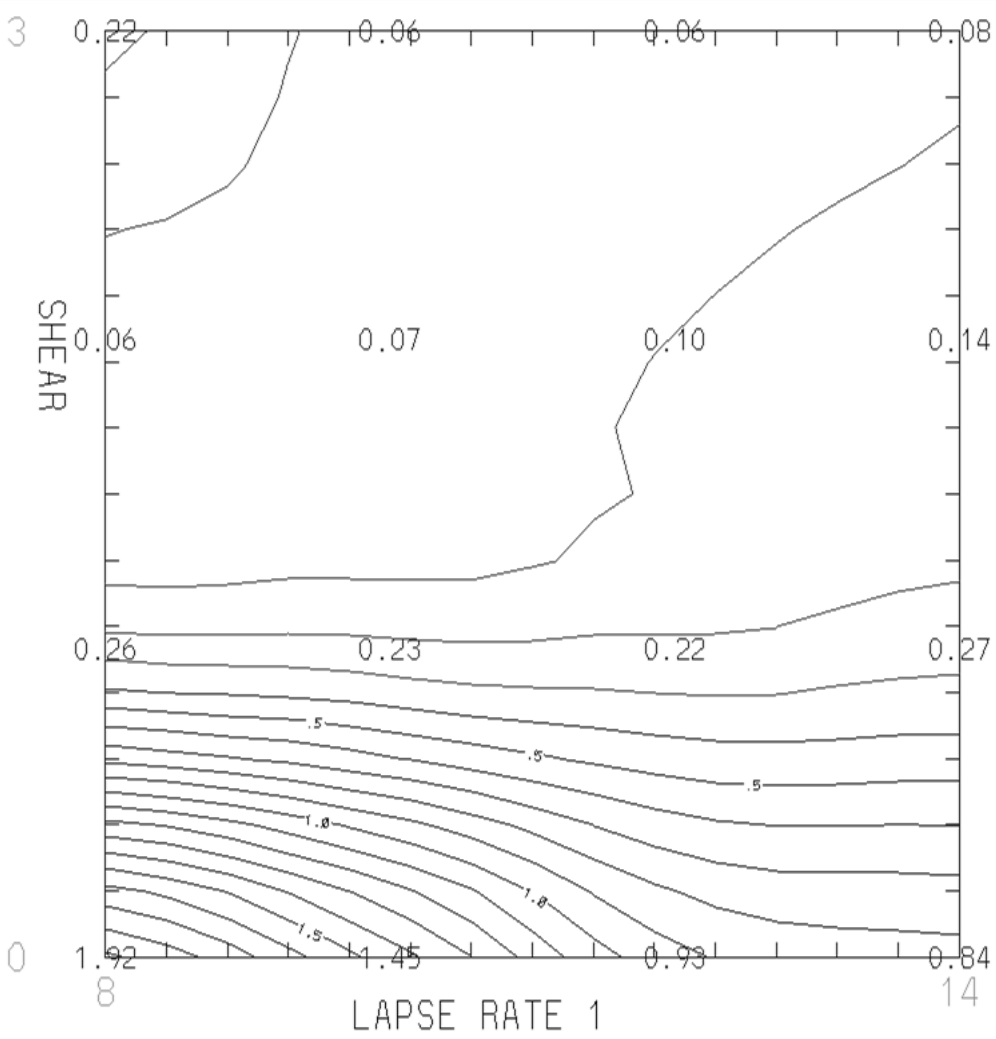

Figure 37. T'_{max} (contoured every 0.1 K) for ΔU = 0-30 m/s, Γ_1=8-14 K/km, Γ_2=0 K/km, H_1=1800 m, and H_2=3000 m. Model output is at point X=110 km for ΔU 0 m/s, X=120 km for ΔU 10 m/s, X=155 km for ΔU 20 m/s and 30 m/s.

The values of the T'_{min} are portrayed in Figure 38. T'_{min} ranges from -0.3 K to -0.1 K for a Γ_1 of 8 K/km, and from -1.5 K to -0.1 K for a Γ_1 of 14 K/km. The most negative T'_{min} was -1.7 K and it occurred with a ΔU of 0 m/s and a Γ_1 of 12 K/km. The most minimum T'_{min} is most dependent on ΔU as perturbations generally become more negative as ΔU decreases. As with the T'_{max}, there is a clear demarcation in perturbations when ΔU is introduced into the model.

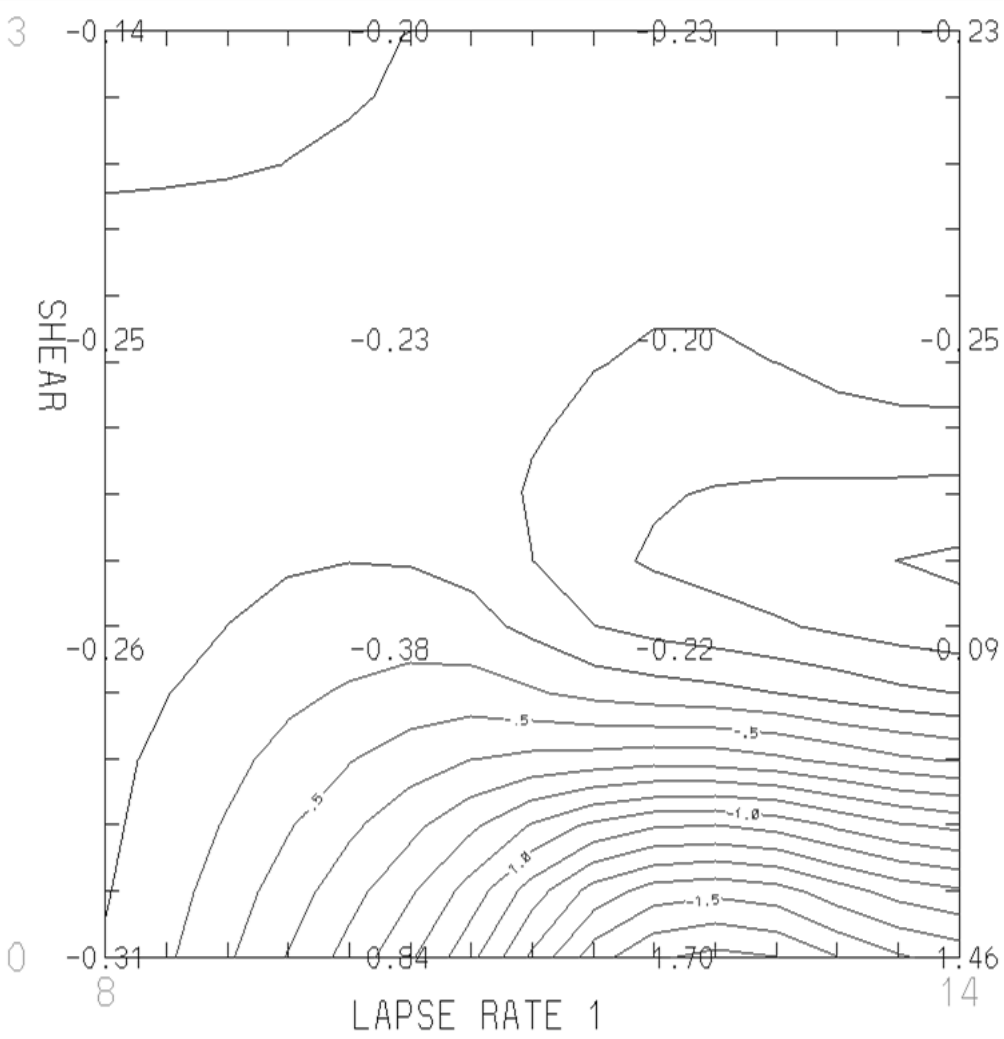

Figure 38. T'_{min} (contoured every 0.1 K) for ΔU = 0-30 m/s, Γ_1=8-14 K/km, Γ_2=0 K/km, H_1=1800 m, and H_2=3000 m. Model output is at point X=110 km for ΔU 0 m/s, X=120 km for ΔU 10 m/s, X=155 km for ΔU 20 m/s and 30 m/s.

The correlation coefficient is portrayed in Figure 39. The value of R was neither highly dependent upon the changes in Γ_1 nor shear. All R values were very close in magnitude. This is evidenced by the model output in Figure 37.

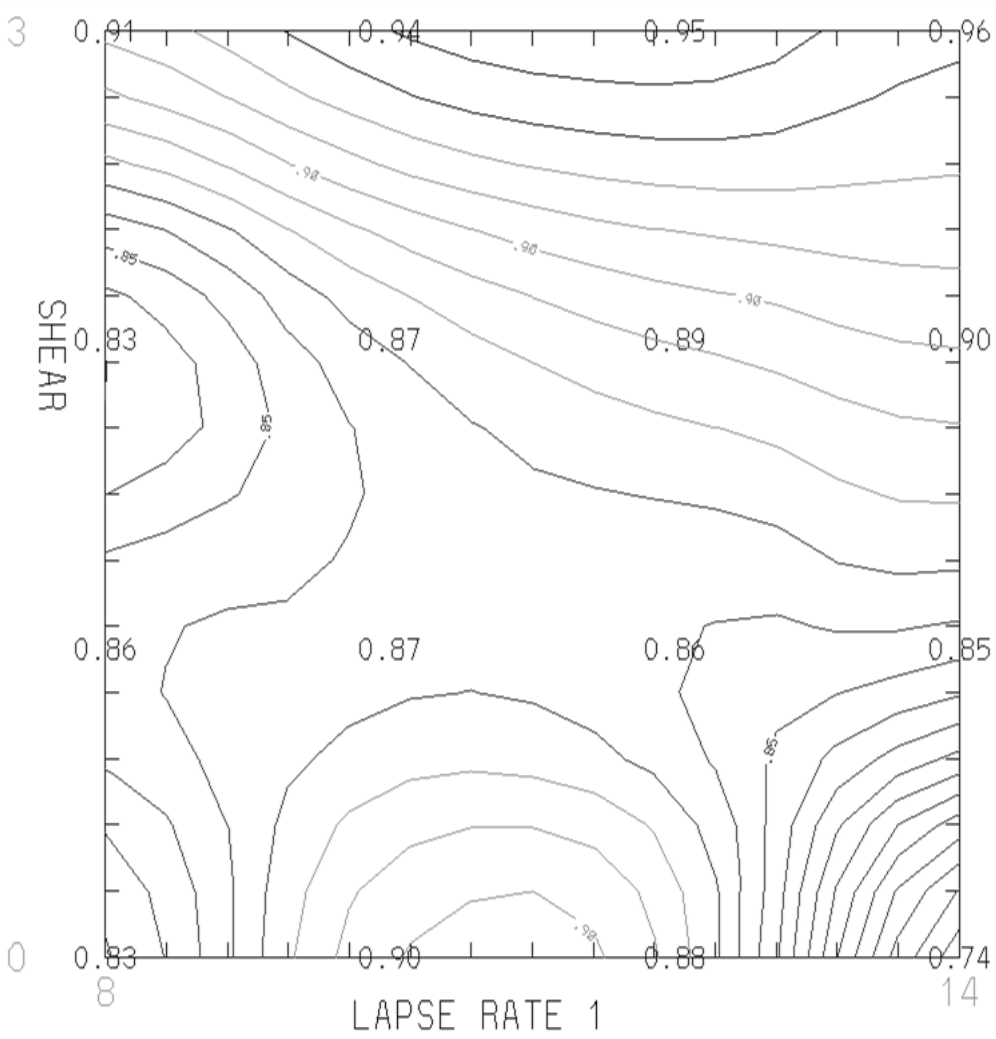

Figure 39. R (contoured every 0.01) for ΔU = 0-30 m/s, Γ_1=8-14 K/km, Γ_2=0 K/km, H_1=1800 m, and H_2=3000 m. Model output is at point X=110 km for ΔU 0 m/s, X=120 km for ΔU 10 m/s, X=155 km for ΔU 20 m/s and 30 m/s.

Generally speaking, ΔU is an important factor in the intensity and structure of MGWs. When ΔU = 0 m/s, the model produces the largest U′ and T′. Larger changes in U′ occur with smaller values of ΔU. P'_{max} tends to increase with less ΔU as well. The largest T′ overwhelmingly occurs with minimal ΔU. The Correlation Coefficient tends be good overall, indicating a strong tendency toward MGW formation and behavior.

With $\Delta U = 0$ m/s, waves are symmetric about the point of origin, while with increasing ΔU, the tendency towards an eastward moving solitary MGW increases with increasing stability. In these simulation examples, there was minimal indication of heat burst response with increases in temperature on the order of 3 K with $\Delta U = 0$ m/s. Heat burst activity decreased with increasing strength of the stable layer. With $\Delta U = 10$ m/s, some heat burst response occurred with a propagating MGW, but heating was less than that of the $\Delta U = 0$ m/s situation. With $\Delta U = 20$ m/s and $\Delta U = 30$ m/s, the behavior was similar and very characteristic of a MGW, with $\Delta U = 30$ m/s cases progressing faster toward the east due to increased environmental shear.

4.4 Heat Burst Activity

In these simulations, it appears that an appreciable increase in temperature sufficient to be considered a heat burst tends to occur when there is minimal ΔU present, H_1 is larger, H_2 is larger, Γ_1 is larger, and Γ_2 is smaller. This appears to be due to the ability of the falling thermal to gain enough momentum to descend to the surface through the stable layer, inducing heating at the surface. The strongest evidence of a heat burst occurred when H_1 was 1300m, H_2 was 2500m, Γ_1 was 14K/km, and Γ_2 was 0K/km. For this case the surface temperature increased about 11°C. This increase in surface temperature held for 2 minutes. An increase of 5°C or higher was held for 8 minutes. This period of 5°C or more began 10 minutes into the simulation and ended 18 minutes into the simulation.

In terms of surface heating, the most important factor is ΔU. When the same atmospheric setup that produced the strongest temperature perturbation was applied in the

other ΔU cases, the temperature perturbation decreased with an increase in ΔU. The values for the four ΔU cases with this setup are displayed in Table 12. For reference, the maximum temperature perturbation for each ΔU set is also listed in the table. A cross-section of temperature is presented in Figure 40 while the surface correlation coefficient and maximum temperature over all times are presented in Figure 41.

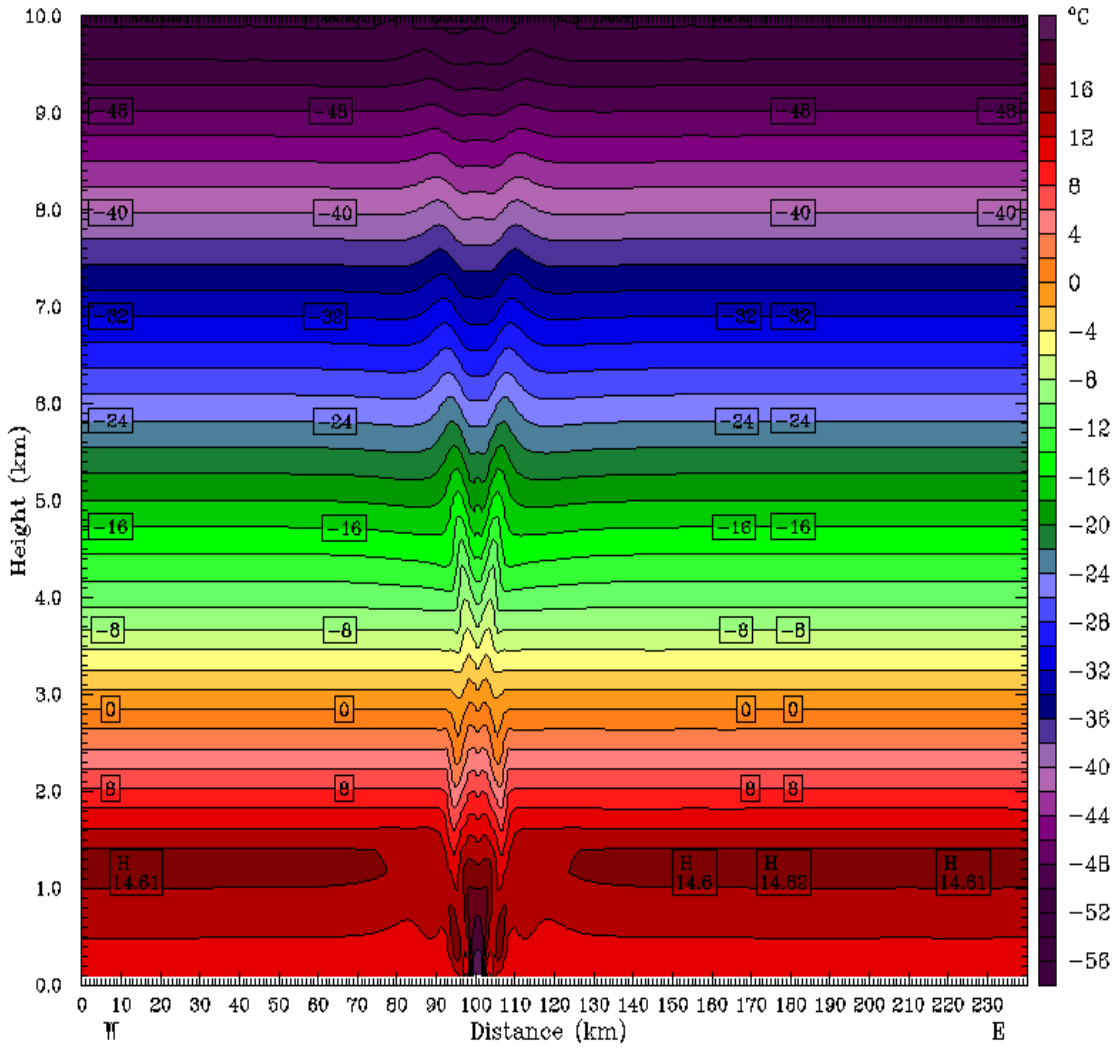

Figure 40. Temperature cross-section of heat burst case at 15 min into the simulation when the most intense heating occurred. Model output is along center of domain at Y=50km. Temperature is plotted in Centigrade.

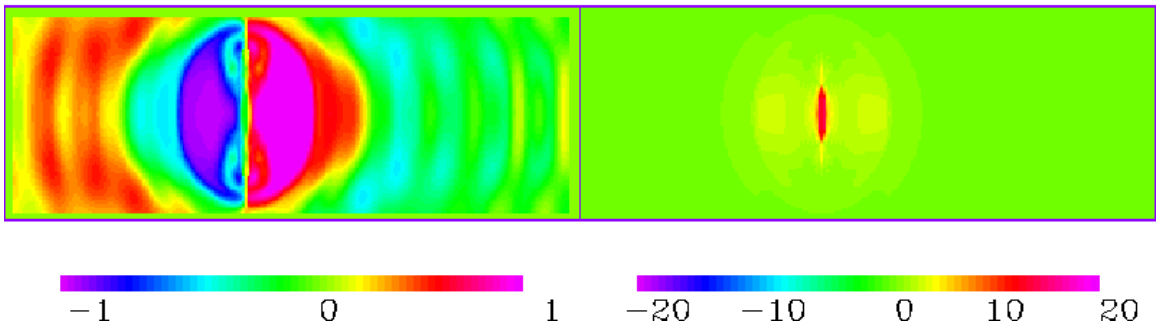

Figure 41. Plan-view model output for the heat burst case. Correlation coefficient is plotted on the left and maximum temperature is plotted on the right at every point over all time.

ΔU	**T'_{max} for maximum in 00m/s case**	**T'_{max} for each ΔU set**
0m/s	11.2°C	11.2°C
10m/s	7.9°C	8.7°C
20m/s	3.4°C	5.0°C
30m/s	1.0°C	2.8°C

Table 2. Maximum temperature perturbation for each ΔU case with an initial sounding configuration in all cases of H_1 = 1300m, H_2 = 2500m, Γ_1 = 14K/km, and Γ_2 = 0K/km.

4.5 General Discussion of the results

Although definite trends do appear in the model results, there are no simple rules for MGW formation, but instead patterns based upon variable values. It is not just lapse rates and their associated atmospheric depths that are important, but also the amount of shear that is present. By varying the amount of shear in the atmosphere at model initiation, differing trends in MGW formation, as indicated by positive correlations between U′ and P′, are revealed.

With no shear in the environment, the best correlations between U′ and P′ tend to occur when Γ_1 is larger, H_1 is larger, Γ_2 is smaller, and H_2 is smaller. When shear is

introduced into the environment, the best correlations between U′ and P′ tend to occur when Γ_1 is larger, H_1 is smaller, Γ_2 is smaller, and H_2 is larger. Between these types of environments, the variables that tend to change in MGW prevalence and formation are the depths of atmospheric layers and the amount of shear within the environment.

When shear is present, the cold thermal has an increasing propagation toward the east that is proportional to ΔU. This horizontal propagation would tend to deflect the impact toward the east, as opposed to an initial environment in which the cold thermal can fall entirely in the vertical. By having a shallower surface layer with less volume upon which to impact in an environment with shear, it is easier for the descending cold thermal to impact with sufficient force and therefore cause a heat burst or microburst response at the surface.

The effects of Γ_1 rest mainly within the realm of surface heating in the form of heat bursts. With the largest values of Γ_1, the possibility of surface heating increases, and is most common when coupled with less amounts of shear. Γ_1 tends to contribute to MGW activity when it is a medium to smaller value (enter value range here in parentheses) as it is less resistant to the action of the thermal. An additional apparent effect of Γ_1 is the progression of the wave. With larger values of Γ_1, MGWs tend to not travel as far from the wave origin, but tend to remain stronger. This shorter spatial movement appears to be due to the inability of the thermal to further impact the stable layer downstream as it meets resistance. However, the increased MGW strength is probably due to the kinetic energy of the thermal being expended in a smaller area as the energy is not allowed to spread further out due to the resistance it encounters.

H_1 allows for better pronounced U′, P′, and T′ if the value of H_1 is smaller. As H_1 increases, it tends to be associated with a decrease in U′, P′, and T′. It appears that having a shallower H_1 layer allows for pressure and wind changes to be more easily observed at the surface. A shallower layer allows for less resistance to the thermal's momentum.

Γ_2 is the most straightforward variable in predictable U′, P′, and T′ behavior. The strongest perturbations tend to occur with a Γ_2 value of 0K/km. This neutral layer aloft allows the thermal to fall unrestricted by environmental conditions and build momentum before impacting the surface stable layer. When Γ_2 increased, all cases showed decreased perturbation magnitude.

The largest influence of H_2 occurs when H_2 is larger. This, when coupled with a Γ_2 value of 0K/km, allows for maximum downward momentum. Additionally, with a larger value of H_2, the surface spread of area that is affected by the thermal tends to be larger. Having a neutral layer allows for the thermal to act unimpeded.

Chapter 5: Conclusions

Mesoscale Gravity Waves (MGWs) are large pressure perturbations that occur behind Mesoscale Convective Systems (MCSs) in summer and over warm frontal surfaces behind elevated convection in winter. They generally form in the presence of a stable layer at the surface. MGWs are associated with damaging winds, moderate to heavy precipitation, and occasional heat bursts at the surface. The forcing mechanism for MGWs in this study was hypothesized to be evaporative cooling occurring immediately behind the convective line. This evaporatively-cooled air generates a downdraft that then depresses the surface-based stable layer and causes pressure decreases, strong wind speeds and MGW genesis. Using the Weather Research and Forecasting Model (WRF) version 3.0, evaporative cooling was simulated using an imposed cold thermal. Sensitivity studies were conducted to examine the response of MGW structure to different thermal and shear profiles where the strength and depth of the surface-based inversion and air layer above it are varied, as well as the amount of vertical wind shear.

MGWs were characterized in terms of response variables, such as wind speed perturbations (U'), temperature perturbations (T'), pressure perturbations (P'), potential temperature perturbations (θ'), and the correlation coefficient (R) between U' and P'. Regime diagrams displaying the results of over 1000 simulations with WRF were used to portray the response of MGWs to the above variables in order to better understand the formation, causes, and intensity of MGWs.

The results of this study indicate that MGW formation is a complex process in the atmosphere that stems from the interaction of several conditions to create the conditions through which noticeable changes in wind and pressure can be observed. Stronger

simulated MGW cases occurs when a smaller value for the lapse rate above the stable layer is coupled with a larger value for the depth of the layer above the stable layer with that lapse rate. The effect of the depth and lapse rate within the stable layer are conditional in that larger values of both are favorable for waves of depression, which are easier to detect, and smaller values are favorable for waves of elevation, which tend to be weaker on the whole. Small enough values of both lowest-layer depth and lapse rate can lead to the formation of microbursts or heatbursts..

Waves of elevation refer to MGWs in which the wave is best described by a correlated increase in wind and pressure. According to the model output presented, waves of elevation tend to occur with a shallow, weak surface layer with a deep neutral layer above. Waves of depression refer to the other extreme in which the wave is best described by a correlated decrease in wind and pressure. These types of waves preferably form when the surface layer is a deep, strong stable layer with a deep neutral layer above. If shear is minimized, a heat burst may also occur with the formation of MGWs with waves of depression.

The results show a more traditional MGW response when a deep, stable surface layer on the order of 1300 – 1800 m and strong shear are present. When the layer is shallower with a depth of 800 m, shear can lead to the development of a traveling microburst, but with subtle surface heating at the surface on the order of 2 – 3 K. However, the behavior is still characteristic of a MGW based upon the correlated changes in surface U′ and P′ in the vicinity of the initial cold thermal impact. With a very shallow surface layer of 300 m, the behavior tends to have traveling microburst characteristics with a correlated change in U′ and P′ with a corresponding decrease in temperature.

The stable layer lapse rate tends to produce stronger MGW activity when it is a smaller value as it provides less resistance to the actions of the sinking cold thermal. Small values also tend to allow the waves to propagate further from the point of origin. Waves formed with weaker surface lapse rates tend to mimic a microburst as opposed to a mesohigh-wake low couplet if the depth of the layer is shallow. However, with larger values of Γ_1, the MGWs are more likely to fit the MGW profile described in Figure 4. MGWs that form with decreased surface lapse rates may also produce surface heating in the form of heat bursts. This is further enhanced by weak or no shear.

MGWs have a visible response to the Shear introduced in the model. When no shear exists, waves tend to be symmetric about the point of thermal impact. As shear increases, the tendency towards a moving solitary MGW increases, especially with increasing stability. Heat burst activity occurred with a neutral second layer, but decreased with increasing strength of the surface stable layer. When shear exceeded 10 m/s, some heat burst activity occurred with a propagating MGW, but the surface heating was less than that of the no shear situation. With strong shear, the behavior was similar to weak shear, although the strong shear cases progressed faster toward the east.

This thesis demonstrated through an idealized modeling study that MGWs can develop as the direct result of evaporative cooling aloft, which does also occur in nature in the wake of the precipitation produced in MCSs. For this reason, the results of this study should aid in enhancing the forecast and detection and prediction of strong MGWs in the operational forecast community.

There are further experiments that can aid in this endeavor. In the future, simulations using a source of constantly cooled air aloft, as opposed to an instantaneously

cooled thermal, should be conducted. This will help further illustrate the effects of prolonged evaporational cooling aloft upon MGW development.

Chapter 6: References

Alameda, J., B. Jewett, R. B. Wilhelmson, A. L. Rossi, and S. D. Hampton, 2008: How the NCSA/LEAD workflow broker manages complex workflows. 9th WRF Users' Workshop, NCAR/MMM, **P11.1**. (http://www.mmm.ucar.edu/wrf/users/workshops/WS2008/WorkshopPapers.php)

Bosart, L.F., and F. Sanders, 1986: Mesoscale Structure in the Megalopolitan Snowstorm of 11–12 February 1983. Part III: A Large-Amplitude Gravity Wave. *J. Atmos. Sci.*, 43, 924–939.

Bosart, L.F., and J.P. Cussen, 1973: Gravity Wave Phenomena Accompanying East Coast Cyclogenesis. *Mon. Wea. Rev.*, 101, 446–454.

Browning, G.L., H.O. Kreiss, and D.W. van de Kamp, 2000: Comments on "Observations of a Mesoscale Ducted Gravity Wave". *J. Atmos. Sci.*, 57, 595–598.

Cram JM, Roger A. Pielke, William R. Cotton (1992) Numerical Simulation and Analysis of a Prefrontal Squall Line. Part II: Propagation of the Squall Line as an Internal Gravity Wave. *Journal of the Atmospheric Sciences*: Vol. 49, No. 3 pp. 209–225.

Eom, J.K., 1975: Analysis of the Internal Gravity Wave Occurrence of 19 April 1970 in the Midwest. *Mon. Wea. Rev.*, 103, 217–226.

Ferguson, H.L., 1967: Mathematical and Synoptic Aspects of a Small-Scale Wave Disturbance over the Lower Great Lakes Area. *J. Appl. Meteor.*, 6, 523–529.

Gaffin, D.M., 1999: Wake Low Severe Wind Events in the Mississippi River Valley: A Case Study of Two Contrasting Events. *Wea. Forecasting*, 14, 581–603.

Haertel, P.T., and R.H. Johnson, 2000: The Linear Dynamics of Squall Line Mesohighs and Wake Lows. *J. Atmos. Sci.*, 57, 93–107.

Houze, R.A., M. Biggerstaff, S. Rutledge, and B. Smull, 1989: Interpretation of Doppler Weather Radar Displays of Midlatitude Mesoscale Convective Systems. *Bull. Amer. Meteor. Soc.*, 70, 608–619.

Jewett, B.F., M.K. Ramamurthy, and R.M. Rauber, 2003: Origin, Evolution, and Finescale Structure of the St. Valentine's Day Mesoscale Gravity Wave Observed during STORM-FEST. Part III: Gravity Wave Genesis and the Role of Evaporation. *Mon. Wea. Rev.*, 131, 617–633.

Jewett, B.F., Robert B. Wilhelmson, Jay C. Alameda and Albert L. Rossi, 2008: Using NCSA/LEADS's Workflow Broker to Study Storm Interaction with WRF. 9th WRF Users' Workshop, NCAR/MMM, **P9.32**. (http://www.mmm.ucar.edu/wrf/users/workshops/WS2008/WorkshopPapers.php)

Johnson, R.H., and P.J. Hamilton, 1988: The Relationship of Surface Pressure Features to the Precipitation and Airflow Structure of an Intense Midlatitude Squall Line. *Mon. Wea. Rev.*, 116, 1444–1473.

Koch, S.E., and C. O'Handley, 1997: Operational Forecasting and Detection of Mesoscale Gravity Waves. *Wea. Forecasting*, 12, 253–281.

Koch, S.E., and L.M. Siedlarz, 1999: Mesoscale Gravity Waves and Their Environment in the Central United States during STORM-FEST. *Mon. Wea. Rev.*, 127, 2854–2879.

Koch, S.E., and P.B. Dorian, 1988: A Mesoscale Gravity Wave Event Observed during CCOPE. Part III: Wave Environment and Probable Source Mechanisms. *Mon. Wea. Rev.*, 116, 2570–2592.

Koch, S.E., and R.E. Golus, 1988: A Mesoscale Gravity Wave Event Observed during CCOPE. Part I: Multiscale Statistical Analysis of Wave Characteristics. *Mon. Wea. Rev.*, 116, 2527–2544.

Koppel, L.L., L.F. Bosart, and D. Keyser, 2000: A 25-yr Climatology of Large-Amplitude Hourly Surface Pressure Changes over the Conterminous United States. *Mon. Wea. Rev.*, 128, 51–68.

Ley, B.E., and W. Peltier, 1981: Propagating Mesoscale Cloud Bands. *J. Atmos. Sci.*, 38, 1206–1219.

Lin, Y.L., and R. Goff, 1988: A Study of a Mesoscale Solitary Wave in the Atmosphere Originating near a Region of Deep Convection. *J. Atmos. Sci.*, 45, 194–206.

Lindzen, R., and K.K. Tung, 1976: Banded Convective Activity and Ducted Gravity Waves. *Mon. Wea. Rev.*, 104, 1602–1617.

Lindzen, R.S., 1974: Wave-CISK in the Tropics. *J. Atmos. Sci.*, 31, 156–179.

Lindzen, R.S., and M. Fox-Rabinovitz, 1989: Consistent Vertical and Horizontal Resolution. *Mon. Wea. Rev.*, 117, 2575–2583.

Parsons, D.B., and P.V. Hobbs, 1983: The Mesoscale and Microscale Structure and Organization of Clouds and Precipitation in Midlatitude Cyclones. XI: Comparisons between Observational and Theoretical Aspects of Rainbands. *J. Atmos. Sci.*, 40, 2377–2398.

Pecnick, M.J., and J.A. Young, 1984: Mechanics of a Strong Subsynoptic Gravity Wave Deduced from Satellite and Surface Observations. *J. Atmos. Sci.*, 41, 1850–1862.

Powers, J.G., 1997: Numerical Model Simulations of a Mesoscale Gravity Wave Event: Sensitivity Tests and Spectral Analyses. *Mon. Wea. Rev.*, 125, 1838–1869.

Powers, J.G., and R.J. Reed, 1993: Numerical Simulation of the Large-Amplitude Mesoscale Gravity-Wave Event of 15 December 1987 in the Central United States. *Mon. Wea. Rev.*, 121, 2285–2308.

Ramamurthy, M.K., R.M. Rauber, B.P. Collins, and N.K. Malhotra, 1993: A Comparative Study of Large-Amplitude Gravity-Wave Events. *Mon. Wea. Rev.*, 121, 2951–2974.

Rauber, R.M., M. Yang, M.K. Ramamurthy, and B.F. Jewett, 2001: Origin, Evolution, and Finescale Structure of the St. Valentine's Day Mesoscale Gravity Wave Observed during STORM-FEST. Part I: Origin and Evolution. *Mon. Wea. Rev.*, 129, 198–217.

Raymond, D. J., 1984: A wave-CISK model of squall lines. *J. Atmos. Sci.*, 41, 1946–1958.

Raymond, D.J., 1976: Wave-CISK and Convective Mesosystems. *J. Atmos. Sci.*, 33, 2392–2398.

Rosenthal, A., and R. Lindzen, 1983: Instabilities in a Stratified Fluid Having One Critical Level. Part I: Results. *J. Atmos. Sci.*, 40, 509–520.

Rosenthal, A., and R. Lindzen, 1983: Instabilities in a Stratified Fluid Having One Critical Level. Part II: Explanation of Gravity Wave Instabilities Using the Concept of Overreflection. *J. Atmos. Sci.*, 40, 521–529.

Schaub, WR (2005) Gravity Waves: Those Important to Operational Weather Forecasting. Forecasting Note. WFO Huntsville, AL. February 28, 2005.

Schmidt, J.M., and W.R. Cotton, 1990: Interactions between Upper and Lower Tropospheric Gravity Waves on Squall Line Structure and Maintenance. *J. Atmos. Sci.*, 47, 1205–1222.

Skamarock, W. C., J. B. Klemp, J. Dudhia, D. O. Gill, D. M. Barker, M.G. Duda, X. Huang, W. Wang, and J. G. Powers, 2008: A Description of the Advanced Research WRF Version 3. NCAR Tech Notes-475+STR

Snyder, C., W.C. Skamarock, and R. Rotunno, 1993: Frontal Dynamics near and following Frontal Collapse. *J. Atmos. Sci.*, 50, 3194–3212.

Stobie, J.G., F. Einaudi, and L.W. Uccellini, 1983: A Case Study of Gravity Waves–Convective Storms Interaction: 9 May 1979. *J. Atmos. Sci.*, 40, 2804–2830.

Testud, J., P. Amayenc, M. Chong, B. Nutten, and A. Sauvaget, 1980: A Doppler Radar Observation of a Cold Front: Three-Dimensional Air Circulation, Related Precipitation System, and Associated Wavelike Motions. *J. Atmos. Sci.*, 37, 78–98.

Uccellini, L.W., 1975: A Case Study of Apparent Gravity Wave Initiation of Severe Convective Storms. *Mon. Wea. Rev.*, 103, 497–513.

Uccellini, L.W., and S.E. Koch, 1987: The Synoptic Setting and Possible Energy Sources for Mesoscale Wave Disturbances. *Mon. Wea. Rev.*, 115, 721–729.

Uccellini, L.W., P.J. Kocin, R.A. Petersen, C.H. Wash, and K.F. Brill, 1984: The Presidents' Day Cyclone of 18–19 February 1979: Synoptic Overview and Analysis of the Subtropical Jet Streak Influencing the Pre-Cyclogenetic Period. *Mon. Wea. Rev.*, 112, 31–55.

Van Tuyl, A.H., and J.A. Young, 1982: Numerical Simulation of Nonlinear Jet Streak Adjustment. *Mon. Wea. Rev.*, 110, 2038–2054.

Yang, M., R.M. Rauber, and M.K. Ramamurthy, 2001: Origin, Evolution, and Finescale Structure of the St. Valentine's Day Mesoscale Gravity Wave Observed during STORM-FEST. Part II: Finescale Structure. *Mon. Wea. Rev.*, 129, 218–236.